Memòria d'investigació de tercer cicle
Programa de doctorat del Departament de Física
Bieni 1993-95

THE INFLUENCE OF VEGETATION ON THE DEVELOPMENT AND STRUCTURE OF MOUNTAIN WAVES

Romualdo Romero March
Departament de Física
Universitat de les Illes Balears
Setembre, 1995

AGRADECIMIENTOS

Al Departamento de Física de la UIB por aceptarme como estudiante de tercer ciclo.

De forma más particular, al Grupo de Meteorología (S. Alonso y C. Ramis) por considerarme desde el inicio como uno más de sus miembros.

Al Dr. E. C. Nickerson del NOAA/FSL (Boulder, CO, USA) por su valiosa colaboración en el desarrollo de esta investigación.

Finalmente, y de forma muy especial, a mi compañera Isabel por su fiel apoyo y comprensión durante el tiempo que duró la elaboración de esta memoria.

PROBLEM DESCRIPTION

The major part of the earth's surface over land is dominated by complex terrain. These surface elements represent only negligible protuberances when they are compared with the earth's radius. However, since the troposphere is only a thin layer with a depth of aproximately 12 km in direct contact with the surface, it is well understood the important role that relief elements play in the processes that occur in that atmospheric layer. Relief elements may exibit a wide range of relevant scales, from small hills to high mountains, and shapes, from almost circular mountains to long barriers. With a planetary scale, the main mountain ranges are even decisive for the world climates. But in general, any mountainous area determines the local meteorology of that region and also supposes an additional degree of complexity for a good forecasting or meteorological study.

Meteorological circulations induced by mountainous terrain may be divided into two categories: those associated with thermally developed wind systems, such as slope or valley winds, and those induced mechanically as a consequence of airflow over mountains, such as blocking, flow splitting, mountain waves, foehn, downslope winds, wave breaking, turbulence etc. This variety of phenomena has important relevance in practical topics, as for example the effects of rugged terrain on diffusion of pollutants for air quality studies, and its understanting supposes a valuable help for forecasters which are daily involved in the prediction of winds over relief systems, downslope windstorms, formation of clouds and thunderstorms by induced lifting, and many other examples.

In particular, a special attention has been paid on mountain waves and associated phenomena in last decades. This is one of the most developed aspects in the ambit of mesoscale meteorology and a good test for any mesoscale numerical model. With the support of observational campaigns, several theoretical studies dealing with linear mountain waves have allowed to understand the regime imposed by topography on the airflow. However, real cases are in fact produced by non linear flows and theory must be completed with numerical studies. These studies help to better describe the different regimes and transitions that occur mainly as functions of topographic dimensions and atmospheric background wind and stability, although some other effects are also important to define the mountain induced circulation. For example, mountain shape, air moisture, earth's rotation, diurnal cycle and boundary layer effects.

This work contributes precisely to this context, since the role of vegetative surfaces through its associated evolving boundary layer is investigated. For a two-dimensional idealized case, the influence of vegetation cover on the development and structure of mountain waves is analysed using a meso-β numerical model. The model includes a detailed representation of surface fluxes and friction which evolve in time as the incoming solar radiation interacts with the soil and vegetation. Simulations with different types of vegetation of a zonal flow over a north-south oriented ridge are presented and examined. The intensity of downslope winds and turbulent kinetic energy structure appears to be especially sensitive to the presence and type of vegetation. Model predicted rainfall is also examined, indicating an enhancement when mountainous areas are covered by conifer forest.

CONTENTS

Chapter 1

INTRODUCTION

1.1 Atmospheric processes over complex terrain

The orography is an essential aspect to determine the meteorology in many areas of the globe. In fact, the climatic characteristics over land regions can not usually be explained whithout considering the orographic configurations of that region. The presence of mountains with their endless varieties of passes, valleys, and slopes provides a breeding ground for a wide range of meteorological phenomena. As a consequence, any serious forecast for a mountainous region must incorporate some schematic model which represents the perturbations induced by the orography.

The influence of orography is not only restricted to local or regional meteorology. Orographic flows encompass all scales of motion and the planetary general circulation including the energy, momentum, heat, and moisture balances is significantly affected by orography. Nevertheless, the atmospheric processes described in this section as well as the type of mountain waves subject of this work, are representative of spatial scales of the order of 100 km and temporal scales of several hours (Mesoscale, Orlanski 1975).

These spatial scales may be completely unobserved by the present synoptic-scale observational network. As a consequence, the development of intensive field experiments has a great importance to explore and understand the action of orography in the airflow. In situ measurements by ground-based measuring systems and by balloons and aircfraft have traditionally been the mainstays of field programs. As an example, the PYREX experiment (Bougeault et al. 1990), was designed to study the dynamical influence of the Pyrenees.

The two most important mechanisms that force orographic flows are thermal and mechanical in nature. Thermal circulations are intimately related to differential heating and cooling associated with diurnal insolation. Mechanical effects are the consequence of an incident airstream that is constrained to follow the topographic surface profile against the restoring forces due to stability. The energy associated with that disturbance is usually carried away from the mountain by steady gravity waves (mountain waves). For small mountains or when the air stability is low, the flow becomes nearly parallel to

the topography. However, for high mountains and stable stratification, the flow exhibits blocking and large-amplitude wave activity.

In a local sense, blocking or flow retardation as it approaches the barrier, can be described as follows: as the stable, low-level air is pushed up the windward slope, it becomes potentially colder than the "ambient" air at that level (Fig. 1.1). This creates a relative high pressure next to the slope, decelerating the flow coming up the slope and often causing it to flow back down the hill. On the other hand, a relative low pressure appears over the lee slope. This configuration of pressure anomalies is known as the orographic dipole.

Large-amplitude mountain waves can be associated with regions of clear-air turbulence that pose a hazard to aviation. At the surface, they produce appreciable downslope winds. Winds sweeping down the slopes of mountain ranges may produce low relative humidities and temperature increases of several degrees in a matter of minutes (foehn effect), as for example the westerly Foehn of the Alps and the Chinook on the eastern slope of the Rockies; or can be cold, for example the Bora, a severe northeasterly downslope wind off the mountains along the Adriatic coast of Yugoslavia.

Similar to surface water waves, lee waves may overturn and be associated with extremely turbulent conditions and downslope windstorms, ranging from a temporary disruption of daily life to destructive consequences. The most spectacular case to be observationally well-documented ocurred on 11 January 1972 along the eastern slope of the Colorado Rockies. On this day, Boulder (Colorado) experienced one of its most severe downslope windstorms with surface winds gusting as high as 220 km/h. Two periods of several hours each contained frequent gusts over 180 km/h. Investigation of the associated mountain waves by Lilly and Zipser (1972) and Lilly (1978) revealed the presence of the powerful wave system depicted in Fig. 1.2.

Most real mountains are highy three-dimensional, providing an additional degree of freedom to the flow with respect to the topographic barrier. One of the most obvious effects of three-dimensional topography as an obstacle to stably stratified flow is the direct deflection of the flow around the mountain (flow splitting), which is associated with recirculations in the lee. Over complex topography, the flow can be channeled and accelerated along the valleys.

Under appropiate synoptic flow, the dynamical influence of a large mountain range is responsible of well known "regional winds". In the mediterranean area, for example, Tramontana from the Gulf of Lyon and Cierzo along the Ebro valley by northern flow, and Autan in the south of France by southern flow, are intense winds caused by the Pyrenees due to effects of channeling.

Nevertheless, the more prevalent situation in mountainous areas is dominated by gentle breezes, typically less than 10 m/s. These milder winds are of thermal origin. The pressure gradient force that provides the driving mechanism arises from the difference between the temperature of the air above heated slope by solar radiation during day (or cooled by longwave radiation into space during night), and that of the free air at the same level.

Two classifications are generally recognized: *Slope winds* and *Valley winds* (see Fig. 1.3), although both wind systems tend to interact. Slope winds, induced by temperature differences between the air adjacent to the slope and the ambient air outside the slope boundary layer, blow parallel to the inclination of the sidewalls, typically upslope by day

and downslope by night. Valley winds blow parallel to the longitudinal axis of a valley as a result of temperature differences that form along the valley or temperature differences between the air in the valley and the air at the same height over the adjacent plain.

In contrast to strong winds and increased turbulence that sweep out and disperse pollutants, low intensity orographic winds can transport harmful gases and particulate matter *en masse*. Since the weaker wind systems are pervasive over much of the year, the problem of anthropogenic pollution is exacerbated over mountainous terrain. For example, the following air pollution situations (see Fig. 1.4) can lead to increased concentrations in rugged terrain (Hanna and Strimaitis 1990):

- *Plume inpingement on high terrain.* High pollutant concentrations occur in stable conditions when the plume trajectory cannot lift over the elevated terrain.

- *Pooling in valleys.* It occurs when the airflow in a valley is cut off from the airflow above the terrain. An inversion is frequently present at ridgetop. Pollutants released into the air at the valley floor can accumulate or "pool" due to the limited dilution rate and the resistance to vertical diffusion.

- *Drainage toward population centers.* At night, if synoptic winds are light and there is strong radiational cooling, persistent downslope drainage winds can develop such that pollutants may be carried downstream toward population centers.

- *Persistence due to channeling.* Any synoptic wind direction with a component along the valley axis will lead to a channeled wind along the valley. Such flow can last for several days, ceasing only with a change in the synoptic pattern. The persistence of the flow leads to long-term pollutant concentration in the valley environment.

On the other hand, thermal and mechanical forcing give rise to convective and stratiform clouds. As a consequence, the prediction of cloudiness and thunderstorms formation must often be formulated in connection with the orographic systems.

Clouds are produced when air becomes saturated and water condenses. Air can be brought to saturation by evaporation from water sources, by cooling by nonadiabatic processes, or by expansion from adiabatic lifting. Mountains disrupt basic airflows to force ascending air currents and therefore can initiate clouds and define the precipitation patterns. In particular, with appropiate large-scale conditions (conditionally unstable temperature lapse rate and advection of moisture by the larger-scale flow), mountain circulations provide the initiation or triggering mechanism for thunderstorms. Two factors must be considered in assesing the ability of a mountain range to produce clouds under a given flow regime:

- *The properties of the atmosphere,* which determine the lifting condensation level (LCL) where air must be lifted to reach saturation, and the level of free convection (LFC) where saturated air becomes positively buoyant.

- *The characteristics of the flow disturbance,* which determine the amount of lifting provided.

However, the two factors are not independent because characteristics of the atmosphere (especially its stability) affect how much lifting the flow will be able to produce, and lifting destabilizes the atmosphere.

If air is lifted to its LCL but not to its LFC, *stable* or stratiform clouds will be produced. If air is lifted to its LFC, *unstable* or cumuliform clouds will be produced.

Thunderstorms formation and precipitation maxima tend to be related with preferred areas of the topography (sometimes referred to as "hot spots") where the lifting induced by the orography is significant. The kinds of lift that a mountain can provide are direct (forced orographic ascent when flow encounters an obstacle); or indirect, as a consequence of blocking, waves or flow deflection (obstacle effects), or when mountain slopes are heated by radiation and develop thermally forced upslope winds. Figure 1.5 summarizes the three types of cloud initiation mechanisms (Banta 1990).

Forced ascent of moist air up the slopes of a mountain barrier can lift the air directly to its LCL or its LFC when such quantities at some inflow level are near or below the level of the ridge top (Fig. 1.5a).

Upslope and up-valley wind systems blow toward the peaks, producing convergence and updrafts near the peaks, where clouds can eventually form (Fig. 1.5b). Depending on external factors such as ridgetop wind direction, cloudiness, and soil moisture, certain areas repeatedly and perhaps predictably act as triggers (Banta 1990).

Obstacle (aerodynamic) effects (Fig. 1.5c) include effects such as upstream blocking, gravity waves, upward motion caused by the turbulent wake, and convergent flow downstream of the mountain range. The flow retardation due to blocking effects results in horizontal mass convergence ahead of the obstacle, and upward air motion. The direct deflection of low-level flow can produce regions of convergence and divergence that lead to updrafts and subsidence, respectively. Two examples of low-level convergence produced by flow deflection are depicted in Fig. 1.6. Upward-motion branches of gravity waves (mountain waves) may be associated with stationary stable clouds. Gravity waves can act together with organized solenoidal, slope-flow circulations and contribute significantly to storm development (Tripoli and Coton 1989).

The next section focuses on the problem of mountain waves. The predictions given by two-dimensional linear theory for small-amplitude mountain waves are presented and discussed. The discussion is extended to non-linear regimes (appropiate for most real mountains), emphasizing the valuable role played by numerical models in the study of realistic mountain waves.

1.2 Two-dimensional mountain waves

A disturbance is created when stably stratified air is forced to rise over a topographic barrier. The energy associated with that disturbance is usually carried away from the mountain by internal gravity waves, specifically referred to as *mountain waves*.

The basic forces that give rise to internal gravity waves are buoyancy restoring forces. If an air parcel is displaced vertically in a stably stratified flow, the buoyancy difference between the parcel and its environment will produce a restoring force, accelerating the parcel back toward its equilibrium position. In the absence of pressure gradient forces and

mean flow, the parcel will oscillate along a vertical axis through its equilibrium position at the Brunt-Väisäla frecuency

$$N = \left(\frac{g}{\theta_0} \frac{d\theta_0}{dz} \right)^{1/2} \tag{1.1}$$

where θ_0 is the vertically varying mean-state potential temperature.

If the parcel is constrained to oscillate along a path tilted off the vertical axis by an angle ϕ, buoyancy forces will produce an identical type of oscillatory motion at the reduced frequency $N \cos\phi$. The pressure gradient and buoyancy forces in an internal gravity wave act in concert to keep air parcels oscillating along a path slanted off-vertical at the angle that matches the frequency of the wave to the resonant frequency $N \cos\phi$. However, it is not possible to support buoyancy driven parcel oscillations at frequencies greater than the Brunt-Väisäla frecuency.

A schematic diagram of an internal gravity wave derived from small-amplitude armonic perturbations about a basic state at rest in a Boussinesq atmosphere (Durran 1990) is plotted in Fig. 1.7. The phase of the wave is constant along the slanting, dashed, and solid lines. Velocity and pressure perturbations (u,w and P) have extrema along the solid lines, where bouyancy perturbations are zero. Buoyancy perturbations have extrema, and velocity and pressure perturbations are zero along the dashed lines. The perturbation velocities, indicated by small arrows in the figure, are allways parallel to the lines of constant phase. Large heavy arrows indicate the direction of phase propagation and the group velocity. With the superposition of a non zero horizontal mean flow, the actual air-parcel trajectories would not follow the slanted paths in Fig. 1.7, but rather wavy lines.

Owing to the nature of the disturbance generator, mountain waves are essentially stationary and propagate energy upwards. However, the momentum flux associated with its internal structure is directed downwards and mountain waves exert a drag on the upper levels of the atmosphere; indeed, the cumulative worldwide effect of mountain-wave drag is believed to have a significant influence on the strength of the mean zonal circulation. It is not strange, therefore, that many efforts have been directed to include some representation (parameterization) of this effect in large-scale numerical models. Drag parameterization schemes based on two-dimensional linear theory have been developed by McFarlane (1987) and Palmer et al. (1986) among others, and other works have dealt with the search of a more realistic parameterization taking into account the enhancement in wave drag under non-linear regimes or the extra degrees of freedom allowed for by three-dimensional orography (Baines and Palmer 1990).

On the other hand, large-amplitude mountain waves can also be associated with regions of clear-air turbulence (CAT) and strong surface winds that blow down the mountain along its lee slope; wind gusts in excess of 50 m/s have been measured in extreme events (see Fig. 1.2).

The orographic forcing on the airflow is usually studied as function of nondimensional numbers. The most important number is the nondimensional mountain height $\hat{h}$, or inverse of the vertical Froude number Fr:

$$\hat{h} = \frac{1}{Fr} = \frac{Nh}{U},$$

where h is the height of the mountain, U is the basic flow speed of the unperturbed atmosphere and N is the Brunt-Väisäla frequency defined by Eq. 1.1 as a measure of the atmospheric stability upstream of the mountain.

The Froude number characterizes the non-linearity of the disturbance. For high values of Fr ($\gg 1$), linear theory can give a good aproximation to the mountain induced flow. However, strong non-linear effects associated with upstream blocking and wave breaking in two-dimensional and three-dimensional flows, and with splitting of the flow around the mountain in three-dimensional cases, arise for sufficiently low Froude numbers.

It should be noted that a real atmosphere has typically a complex vertical structure for $U(z)$ and $N(z)$, and the introduction of a single Froude number based on constant profiles for U and N is not possible. Even in the linear limit, analytical solutions are not possible for atmospheres with complex structure.

Simple arguments from 3-D linear theory, as given by Smith (1988, 1989a), suggest that, in the transition from high to low Froude number, the flow is subject to two opposing effects: (i) an increase in wave amplitude, leading to wave breaking aloft, downstream of the mountain; and (ii) a supression of wave activity with the splitting of the flow around the mountain.

A nondimensional number measuring the three-dimensionality of the obstacle is the aspect ratio a_y/a_x. In the simplest case in which the topography is symetric and the basic current is directed along some of the axis of symetry, a_x represents a characteristic width scale along that direction and a_y is the width scale along the perpendicular direction. The presence and competence of regimes (i) and (ii) above mentioned make the three-dimensional problem more complicated, and this will not be treated here. That is, we are interested in the two-dimensional case of an infinite mountain ridge with $a_x = a$ and $a_y = \infty$. Rigorously, another constraint to be applied in the two-dimensional hypothesis is that the Rossby number $R_o = U/fa$ (f: Coriolis parameter) is large enough to neglect the Coriolis force.

Another important nondimensional number, which characterizes the validity of the hydrostatic aproximation, is Na/U (inverse of the horizontal Froude number). If that number is high ($\gg 1$), the horizontal scale of the perturbation is appreciably larger than its vertical scale and the hydrostatic aproximation is valid. For small values of the nondimensional number, nonhydrostatic effects should be considered. Although nonhydrostatic effects are also discussed in the presentation, the study developed in this work lies in the ambit of β-mesoscale meteorology and treats only with hydrostatic mountain waves.

1.2.1 Linear theory

Linear solutions for small-amplitude mountain waves that strongly resemble observed waves have been obtained and discussed in previous works (Queney et al. 1960; Smith 1979; Gill 1982; Durran 1986). Of course, analytical solutions can be only obtained for idealized terrain profiles and simple atmospheric vertical structures (uniform properties or atmospheres structured in a few uniform layers). We will focus our discussion for uniform basic flow U and stability N.

For an inviscid, adiabatic and Boussinesq atmosphere, the two-dimensional linearized governing equations derived from stationary small-amplitude perturbations about the

hydrostatically balanced basic-state can be reduced to a single equation for the vertical velocity:

$$\frac{\partial^2 w}{\partial x^2} + \frac{\partial^2 w}{\partial z^2} + l^2 w = 0, \tag{1.2}$$

where l is the Scorer parameter ($l^2 = N^2/U^2$).

Solutions to Eq. 1.2 may be written in the form

$$w = Re\left[A \exp^{i(kx+mz)} + B \exp^{i(kx-mz)}\right],$$

where Re denotes the real part, A and B are complex coefficients, and substitution in Eq. 1.2 gives

$$m = (N^2/U^2 - k^2)^{1/2}.$$

For a pure sinusoidal terrain profile $z_s = h \cos kx$, the solution for $w(x, z)$ can be easily obtained imposing appropiate boundary conditions (Durran 1990):

1. At the lower boundary, the velocity normal to the topography must vanish. This condition is approximated, to the same order of accuracy as the linearized equations, by
$$w(x, 0) = U \frac{\partial z_s}{\partial x}.$$
2. As $z \to \infty$ the "radiation condition" is applied, which requires that all waves at an arbitrarily great height above the mountain must be transporting energy away from the mountain.

The above conditions require $B = 0$ and $A = iUhk$, leading to the solution

$$w(x, z) = \begin{cases} -Uhk \exp^{-\mu z} \sin kx, & Uk > N \\ -Uhk \sin(kx + mz), & Uk < N \end{cases} \tag{1.3}$$

where μ is the real number $(k^2 - N^2/U^2)^{1/2}$.

In the case $Uk > N$ the waves decay exponentially with height (evanescent waves) and the wave crests are aligned vertically. The waves decay away from the forcing because the intrinsic frequency exceeds the Brunt-Väisäla frequency and there is no way for buoyancy restoring forces to support the oscillation. In the case $Uk < N$, buoyancy restoring forces can support the oscillation. The waves propagate vertically without loss of amplitude and the wave crests tilt upstream with height at an angle $\phi = \cos^{-1}(Uk/N)$.

The solution to Eq. 1.2 for a more realistic terrain profile as an isolated ridge requires the use of Fourier transforms. Each component of the Fourier transformed vertical velocity $\tilde{w}(k, z)$ must satisfy the Fourier transform of the governing equation 1.2

$$\frac{\partial^2 \tilde{w}}{\partial z^2} + \left(l^2 - k^2\right) \tilde{w} = 0. \tag{1.4}$$

The solution to Eq. 1.4, subject to appropiate upper and lower boundary conditions, is

$$\tilde{w}(k, z) = ikU \tilde{z_s}(k) \exp[i(N^2/U^2 - k^2)^{1/2} z]. \tag{1.5}$$

This equation is the complex analog of Eq. 1.3; therefore, each component $\tilde{w}(k,z)$ of the transformed vertical velocity is identical to the velocity forced by an infinite series of sinusoidal ridges having wavenumber k and amplitude $\tilde{z_s}(k)$ (k-component of the Fourier transformed topography). Thus, the previous discussion based in the relation beween Uk and N is also applicable in terms of $\tilde{w}(k,z)$. The only complication arises from the requirement that after $\tilde{w}(k,z)$ is determined, the total vertical velocity $w(x,z)$ must be obtained by computing an inverse Fourier transform.

Queney (1948) calculated solutions for the waves generated by the "Witch of Agnesi" terrain profile (this bell-shaped function is commonly used in mathematical physics because of its simple Fourier transform):

$$z_s = \frac{ha^2}{a^2 + x^2}. \tag{1.6}$$

In our problem, the Fourier transform of the terrain profile determines the relative weight attached to each individual wavenumber according to Eq. 1.5. For a very narrow mountain, $Ua^{-1} \gg N$; the profile is dominated by wavenumbers greater than N/U, and the mountain primarily forces evanescent waves (Fig. 1.8a). For a wide mountain $Ua^{-1} \ll N$; the dominant wavenumbers are less than N/U, and the waves propagate vertically with lines of constant phase tilting upstream (Fig. 1.8b).

The wide mountain limit is equivalent to the hydrostatic limit. It should be emphasized the characteristic feature of hydrostatic mountain waves: wave crests are only present in the air flowing over the mountain (see streamlines in Fig. 1.8b). Additional crests appear downstream from the mountain (Queney 1948) if nonhydrostatic effects are significant ($Ua^{-1} \sim N$).

Since the flow velocity is given by the gradient of the streamlines, Fig. 1.8b serves also to show the general wind structure for hydrostatic mountain waves. Alternate tilted regions of enhanced and decreased wind speed exist over the barrier, and in contrast with the upslope, the lee of the mountain is affected by appreciable winds at low levels. As a consequence of the upstream tilting of the wave, the vertical flux of horizontal momentum averaged over the mountain is directed downward for all z, since the strongest horizontal winds occur where the vertical velocity is negative.

1.2.2 Nonlinear effects. Role of numerical models

The previous linear solution for the two-dimensional mountain wave shows that the height of the mountain plays only the role of an amplitude factor. However, when the height of the mountain is increased (Fr decreases), the wave amplitude enhances and nonlinear interactions are important. In particular, for sufficiently high obstacles the flow may be characterized by:

- *Breaking.* High mountains can force internal waves of sufficient amplitude to produce flow stagnation aloft over the lee of the mountain, leading to wave breaking. Beyond that critical point there is even overturning of the flow and the temperature profile is unstable in the breaking region. Breaking enhances the wave drag, develops important turbulence in the middle troposphere, and is reflected at the surface with downslope windstorms.

- *Blocking.* For still higher barriers (smaller Fr), the flow decelerates enough to produce a second point of stagnation on the windward slope. In the case of three-dimensional mountains, the stagnation would be accompanied by flow splitting.

As interpreted by Smith (1989b), stagnation is associated with increasing pressure along a streamline caused by lifting and positive density anomalies aloft.

By definition, linear theory is restricted to the study of disturbances created by small mountains ($Nh/U \ll 1$). Therefore, finite-amplitude mountain waves and the above effects which appear for $Nh/U \sim 1$, do not belong to its domain of validity.

The simplest theoretical model to solve the problem of two-dimensional finite-amplitude mountain waves was developed by Long (1953). He showed that there exists a simple steady state solution for the fully nonlinear problem of stratified Boussinesq flow over an obstacle of finite height. When the incident flow has constant static stability N and horizontal velocity U, the streamline deflection field satisfies the same linear Helmholtz equation as does that for infinitesimal perturbations. In the Boussinesq framework this equation takes the simple form

$$\frac{\partial^2 \eta}{\partial x^2} + \frac{\partial^2 \eta}{\partial z^2} + \frac{N^2}{U^2}\eta = 0, \tag{1.7}$$

where $\eta(x, z) = z - z_0$ is the streamline deflection from its far upstream, undisturbed height z_0.

In contrast with the linear theory, where the lower boundary condition is imposed as $\eta(x, z = 0) = z_s(x)$, Long's equation must be solved with the correct boundary condition

$$\eta[x, z = z_s(x)] = z_s(x) \tag{1.8}$$

in order to account effectively for the nonlinear effects in the solution.

Analytical solutions of the Long's equation 1.7 with the exact nonlinear boundary condition 1.8 exist for some particular topographies such as semi-circular and semi-elliptic terrain profiles. For more realistic profiles, the equation must be solved numerically by spectral, iteratives techniques (Bacmeister 1987; Laprise and Peltier 1989). Miles and Huppert (1969) obtained the value of $Nh/U = 0.85$ as the critical value for the overturning of the streamlines (wave breaking) of hydrostatic waves launched by flow over a mountain with the "Witch of Agnesi" shape. The nonhydrostatic effets tend to increase the critical height necessary to develop the unstable region in altitude (Bacmeister 1987).

However, as noted by Smith (1977), the assumption of constant U and N in the Long's model places a special constraint on the nonlinear interactions possible in steady flow, and caution should be exercised in generalized the description of finite-amplitude mountain waves to more realistic atmospheric profiles. As concluded by Durran (1986) from a series of simulations with an atmosphere structured in two layers, the sensitivity of the solution to nonlinear processes is greatly enhanced by the presence of an interface of U and N.

However, to account for structured atmospheres for analytical purposes is very difficult. Thus, the use of numerical models has a great importance in the study of finite-amplitude mountain waves and is essential to develop or confirm any theoretical model of strong nonlinear regimes associated with wave breaking, downslope windstorms and blocking. Realistic atmospheric and terrain profiles can be easily introduced in a numerical model,

and the sensitivity of the orographic disturbance in response to certain control parameters can be isolated by performing several numerical simulations. By this process, numerical models are a key instrument to fill out the regime diagrams of the interaction flow-topography for a complet range of atmospheric profiles and topographic dimensions.

On the other hand, the study of the role exerted by some secondary factors, such as earth's rotation, diabatic processes, viscosity, diffusion, turbulence, atmospheric moisture and boundary layer effects (the last two form the basis of this work), can be only assumed with the aid of numerical models.

1.3 Scope of the study

In recent years, studies have been carried out dealing with the influence of soil and vegetative characteristics on the development of mesoscale circulations. These studies have emphasized the important role played by soil texture through its influence on surface moisture availability, but have indicated that for soils with an adequate water supply, sufficiently dense vegetative cover becomes the dominant surface factor in the evolution of the planetary boundary layer (PBL) (Pinty et al. 1989). However, soil properties must be taken into account in cases of sparse vegetation or when the soil is subjected to a water deficit. In order to isolate the effects of such surface inhomogeneities, those simulations have emphasized the simplest conditions: flat terrain, clear sky situations and/or an unperturbed synoptic environment. With those conditions, thermally induced circulations such as sea breezes or circulations associated with differential heating between zones of different soil or vegetative properties have been simulated (Mahfouf et al. 1987; Pinty et al. 1989).

On the other hand, idealized or real cases of flows over complex terrain have been used in numerical models to describe atmospheric perturbations induced by orography. Simulations with simplified orography and atmospheres of linear and non-linear flows over mountains have extended the theoretical concepts of mountain waves and have proved useful in testing the correctness and sensitivity of the model approach (e.g. Klemp and Lilly 1978; Anthes and Warner 1978; Mahrer and Pielke 1978; Nickerson et al. 1986). Successful simulations of the well documented 11 January 1972 windstorm in Boulder, Colorado (see Fig. 1.2), have been carried out (e.g. Klemp and Lilly 1978; Durran and Klemp 1983), and have indicated that the inclusion of surface frictional effects gives a more realistic development and evolution of downslope winds (Richard et al. 1989). The damping effects of atmospheric water vapor and liquid water on the development of mountain waves have also been considered (Durran and Klemp 1983); however, sensitivity studies have not been presented which demonstrate the response of mountain waves to different specifications of surface properties.

In the present work, two-dimensional numerical experiments are carried out using a meso-β model with a detailed representation of the soil-atmosphere interface to study the effects of different vegetative covers on the dynamical and thermodynamical structure of hydrostatic atmospheric waves induced by a bell-shaped ridge. Surface fluxes and model-predicted rainfall are also examined.

Next chapter contains a detailed description of the atmospheric numerical model as

well as of the associated sub-models which parametrize cloud microphysics, radiative fluxes, surface fluxes of momentum, heat and moisture, and surface balances of energy and water. Chapter 3 presents the particular conditions for the individual experiments and the results of the simulations including the wave structure, an examination of different terms comprising the energy balance at the surface, as well as an examination of the surface pressure drag and the model-predicted rainfall. The work is finally closed with the conclusions.

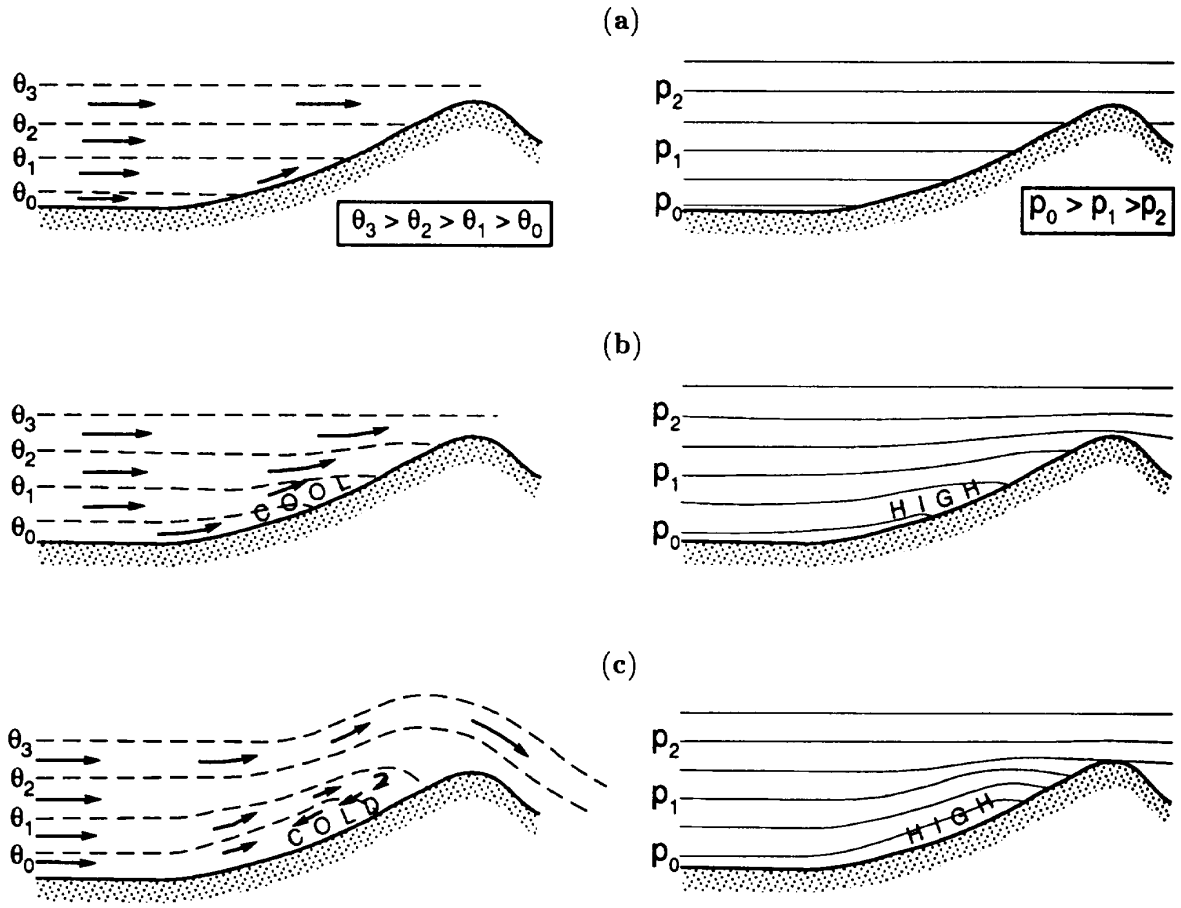

FIG. 1.1. Two-dimensional, $x - z$ potential temperature (left) and pressure (right) cross-sections illustrating blocking. (**a**) Cold air at lower levels in the approach flow is pushed up the slope by the winds. (**b**) Since the air along the slope is cooler than ambient air at each level, the pressure becomes higher along the slope. This adverse pressure gradient retards the flow up the slope or (**c**) may even turn it back down the slope.

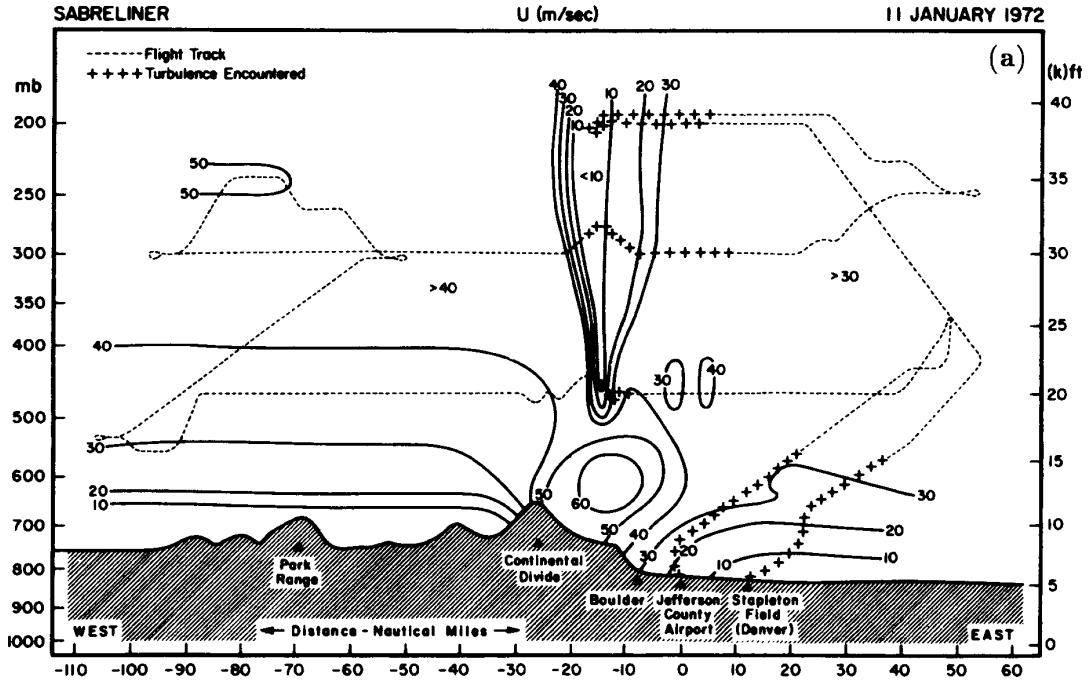

FIG. 1.2. (a) Analysis of westerly wind component (m/s) along an east-west line through Boulder (Colorado). (b) Analysis of the potential temperature field (K). The analysis are based on aircraft flight data and sondes taken January 11, 1972. The dashed lines show aircraft track, with periods of significant turbulence shown by pluses.

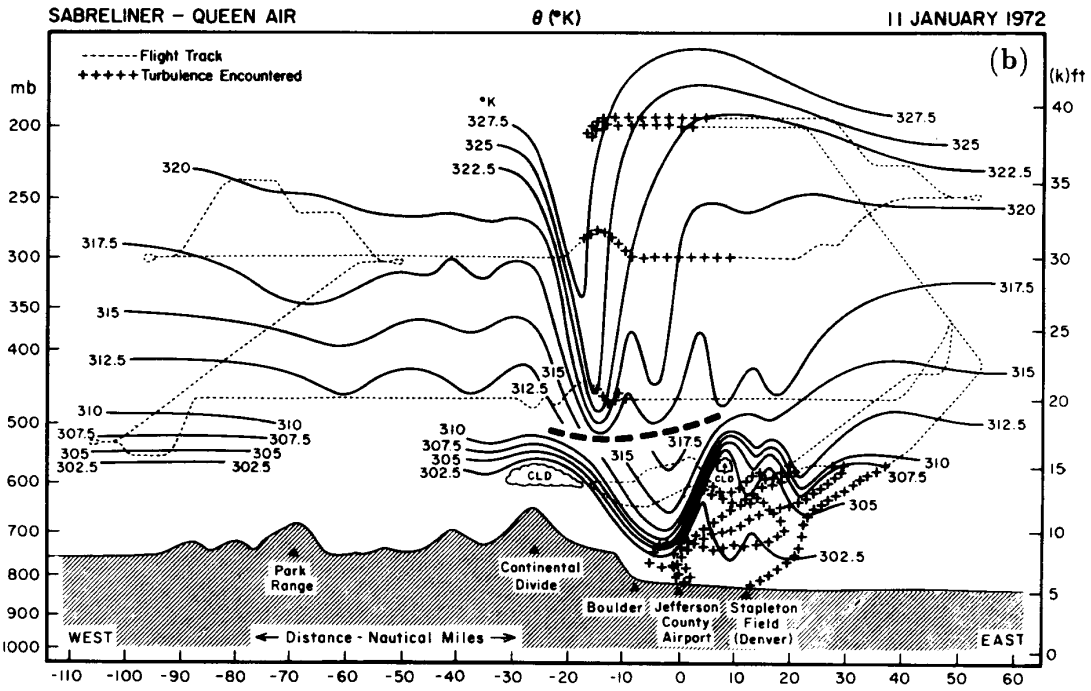

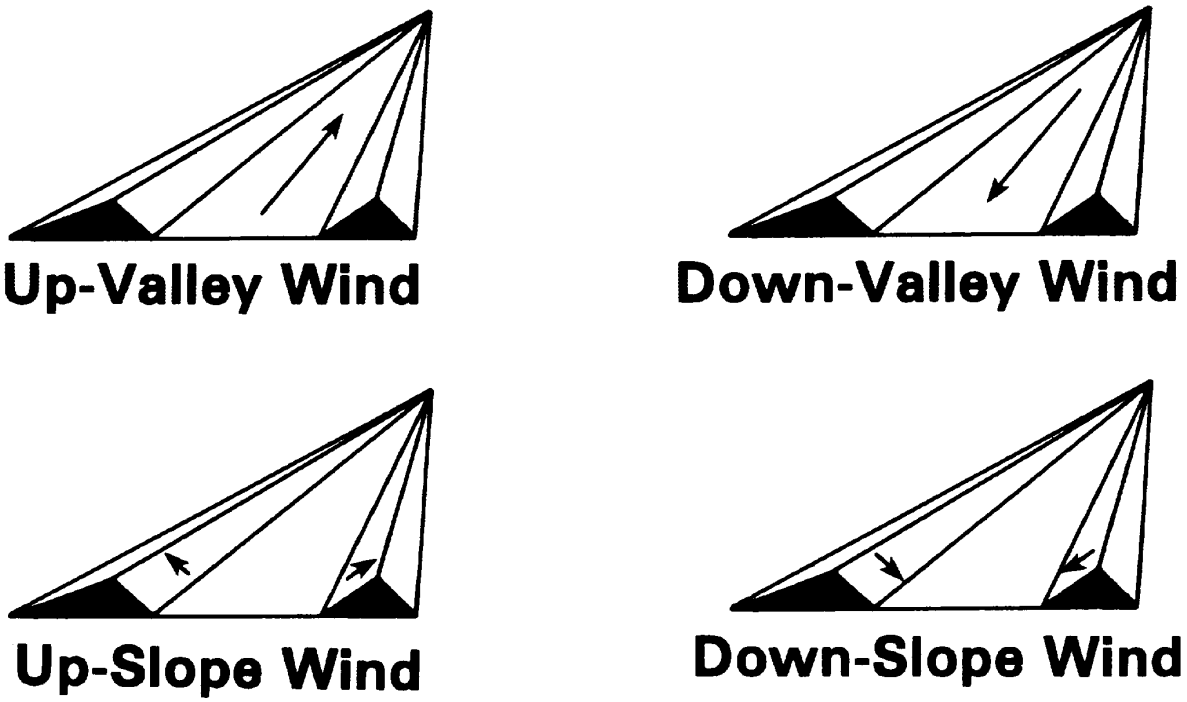

FIG. 1.3. Classification of thermally developed wind systems.

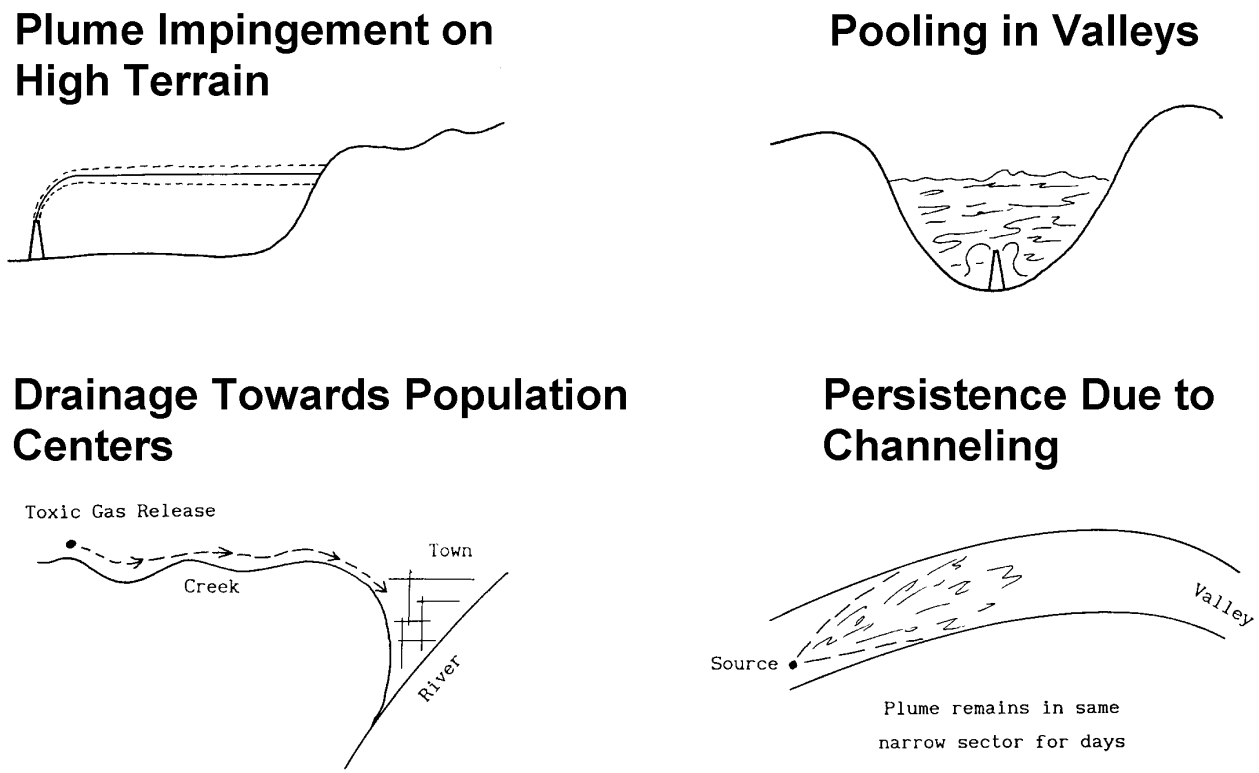

FIG. 1.4. Four types of scenarios that lead to high air pollution concentrations in rugged terrain.

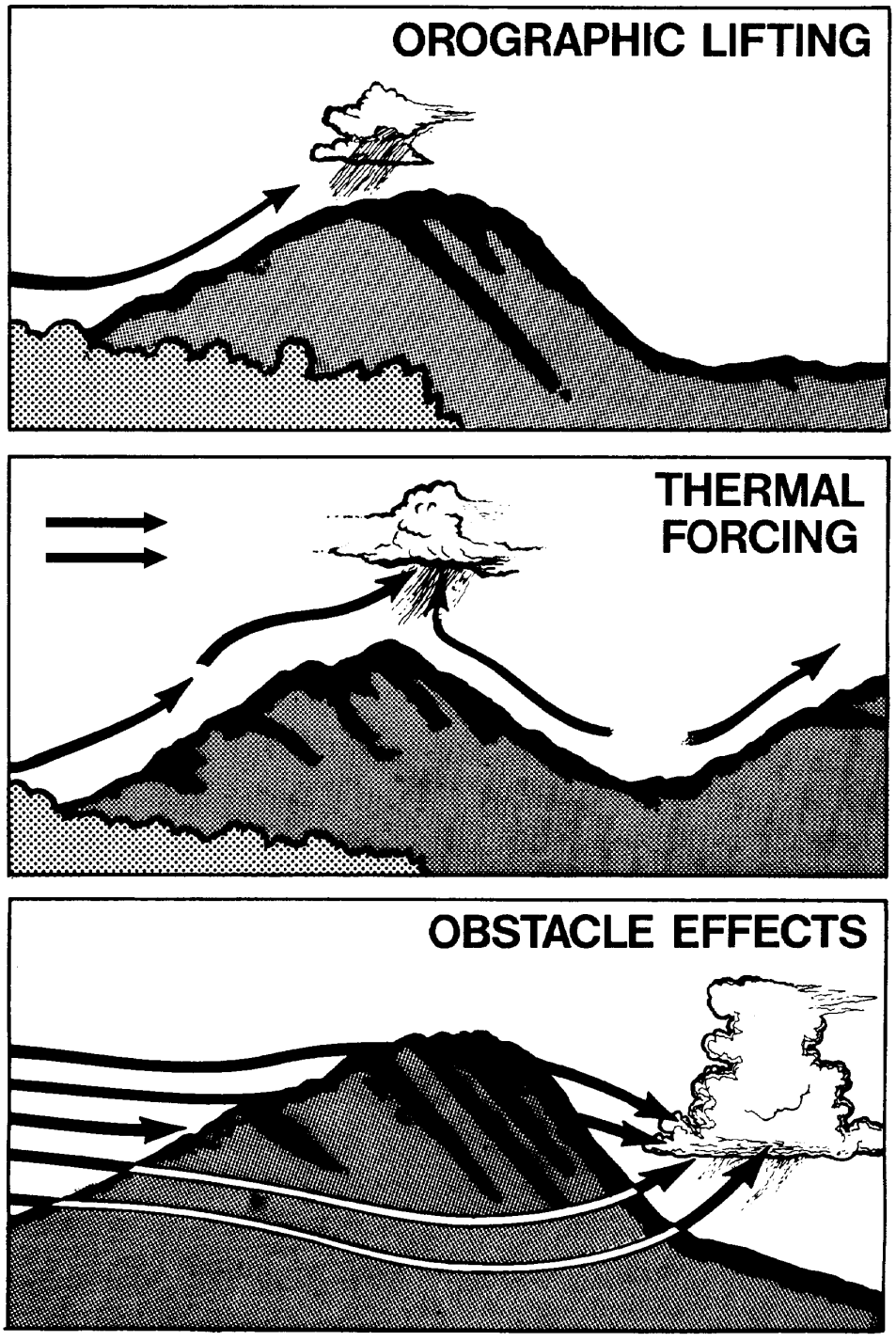

FIG. 1.5. Orographic clouds. Three types of initiation mechanism.

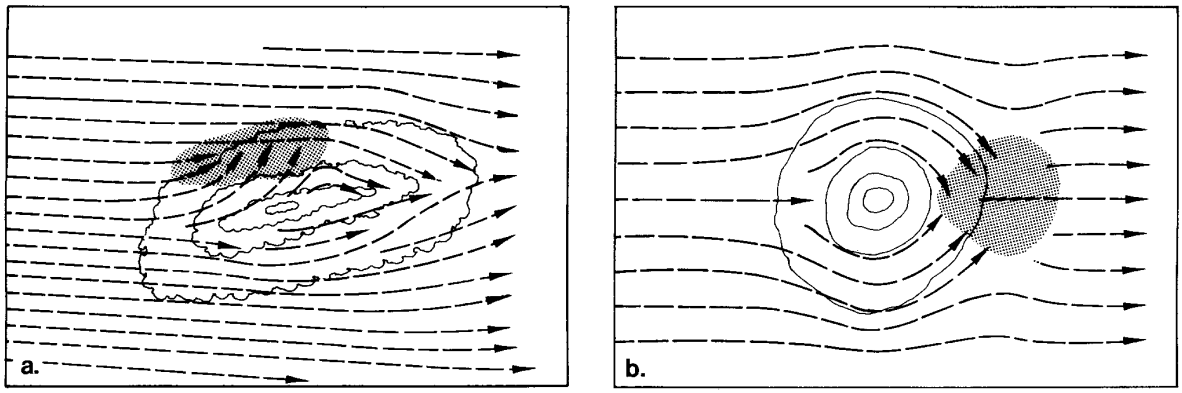

FIG. 1.6. Horizontal flow patterns showing obstacle effects: (**a**) flow deflection by a mountain range nearly parallel to the flow, and (**b**) confluence in the wake of an obstacle. Shaded areas indicate the regions of maximum convergence.

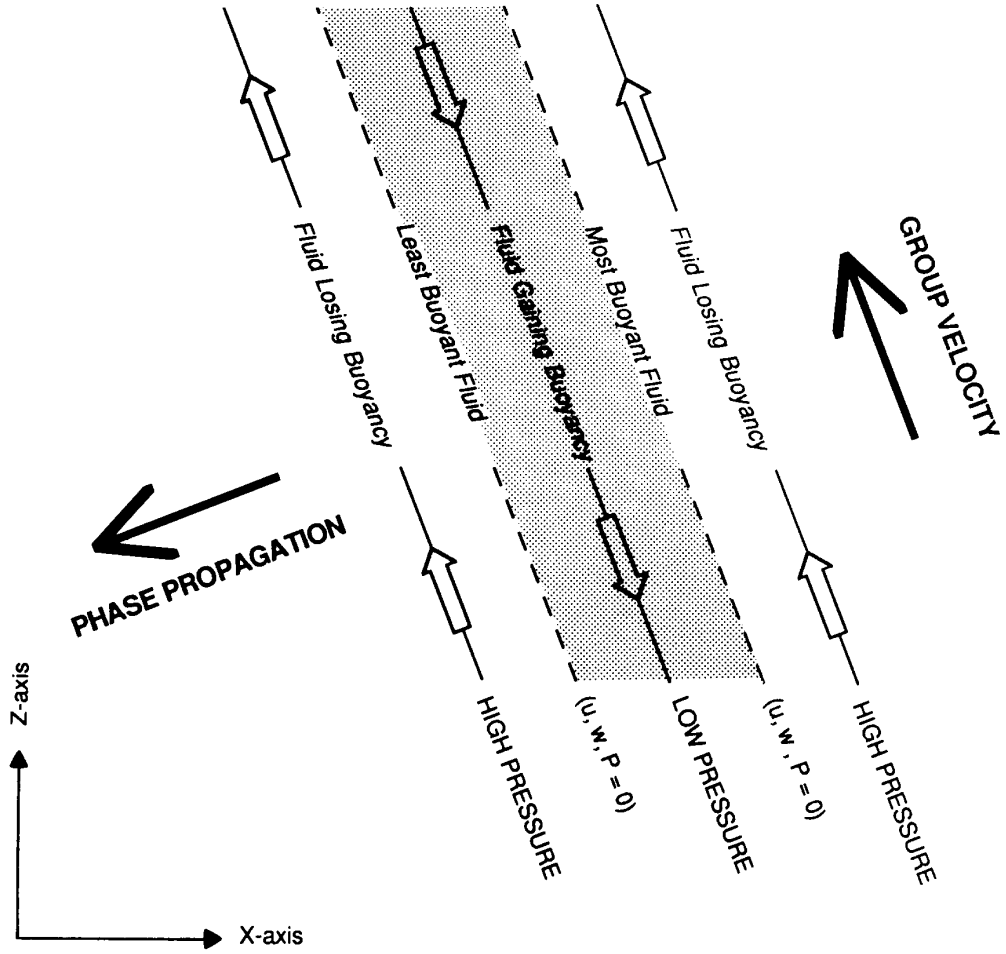

FIG. 1.7. The instantaneous distribution of velocity, pressure, and buoyancy perturbations in an internal gravity wave.

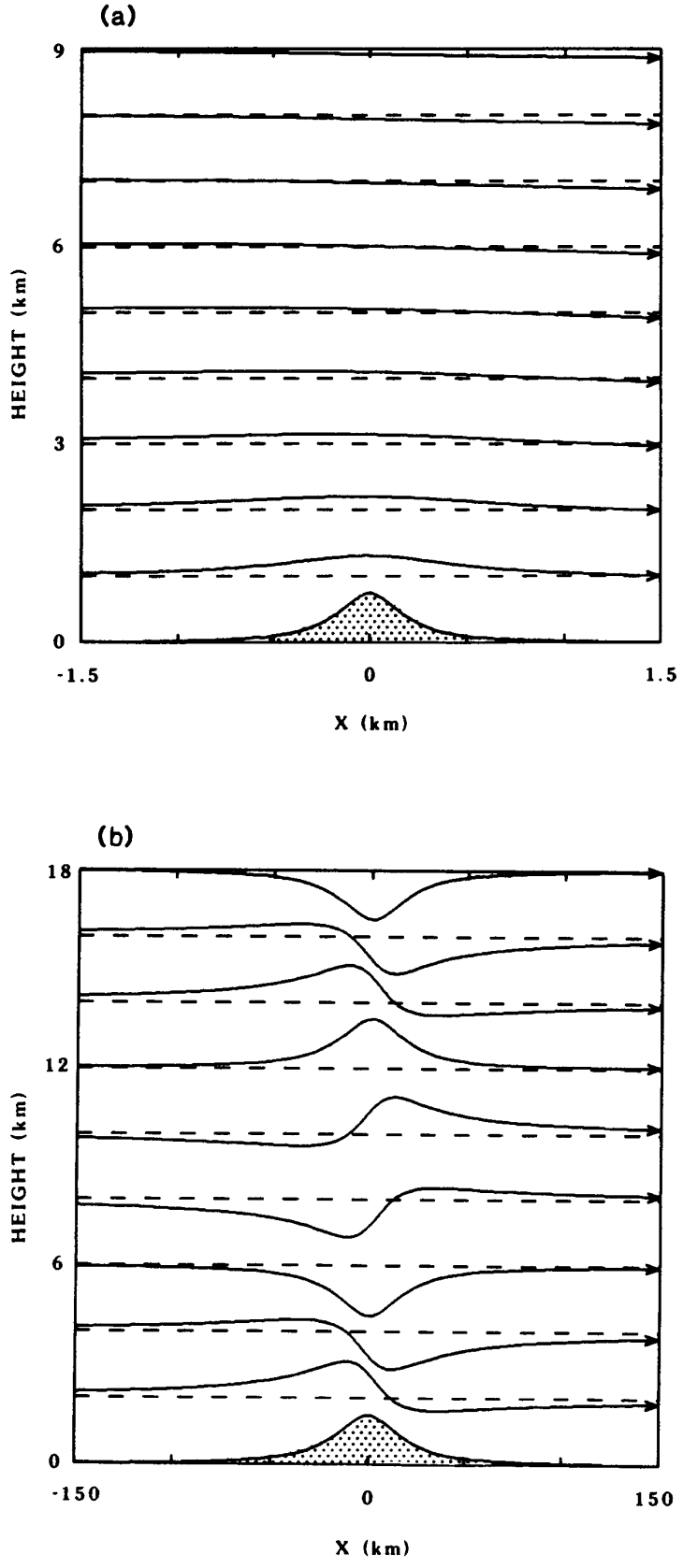

FIG. 1.8. Streamlines in steady airflow over an isolated bell-shaped ridge when (**a**) $Ua^{-1} \gg N$, or (**b**) $Ua^{-1} \ll N$.

Chapter 2

MODEL DESCRIPTION

The atmosphere is a hydro and thermodynamical system that can be analysed by equations which contain time derivatives and therefore allow potential prognostic abilitiy of the future states. The essential governing equations are the momentum or dynamical equations and the conservation relations for mass (continuity equation), entropy (thermodynamic equation) and water vapour (humidity equation). The whole system of equations is closed by the equation of state which in the case of the atmosphere is accurately represented by the ideal gas law; but other formulations arise usually to parameterize some secondary processes such as radiative fluxes across the atmosphere, turbulence, microphysical transformations between water constituents, latent and sensible heat fluxes at the surface, loss of momentum due to roughness, etc.

Unfortunately, the treatment of that system of equations is not simple and only for idealized cases analytical solutions exist. However, for many purposes (for example to dessign a numerical model), the primitive equations can be simplified and/or reduced by neglecting some irrelevant terms. This is done through a scale analysis of the different terms based on the spatial and time scales of the atmospheric process in study. With such technique, terms with appreciably smaller magnitudes than the leading terms can be supressed. Among the typical aproximations sometimes valid, there are the geostrophic aproximation which balances the Coriolis force with the pressure force in the horizontal motion equations, the hydrostatic aproximation which balances the vertical pressure gradient with the gravitational force, and the inviscid, adiabatic, anelastic or Boussinesq assumptions. The characteristic scale of the simulated atmospheric system determines also the necessity and degree of complexity of the parameterizations of subgrid scale physical processes such as those mentioned in last paragraph.

The real atmosphere manifests a wide range of motion scales, i.e, many processes with different characteristic wavelengths and periods. The classical division of that spectra, which extends from ultra-long waves of climatological scale to little eddies produced by roughness in the scale of centimetres and fractions of second, is given by the classification of macro, meso and micro-scales. The macroscale is basically quasi-geostrophic and hydrostatic. The mesoscale is non-geostrophic and hydrostatic, and the microscale is non-geostrophic, non-hydrostatic and turbulent. Spectral analysis of many meteorological observations suggest a minimum of energy density for the mesoscale, whereas both microscale and macroscale represent a maxim (Atkinson 1981). Nevertheless, mesoscale

circulations are very important as a vital link in the atmospheric energy cascade from very large to very small scales (Robinson 1967).

The three motion scales are of course subdivided in other subescales. In the case of the mesoscale, the subclassification of meso-α (fronts, hurricanes ...) with horizontal scales between 200 and 2000 km, meso-β (for example mountain produced disturbances) with scales between 20 and 200 km, and meso-γ (thunderstorms, urban effects ...) with scales smaller than 20 km but greater than 2 km, is often defined.

The numerical model presented in this chapter, used as the main research tool in the development of the study, is a meso-β model and therefore is appropiate to simulate mountains waves. Furthermore, the parameterizations of short and longwave radiation, surface fluxes, warm microphysics and planetary boundary layer (PBL), allows to study the effect of diurnal cycle, air moisture and surface characteristics. In fact, the same model has been used in previous works to simulate phenomena such as orographic enhancement of rain and clouds (Nickerson 1979; Richard et al. 1986), mesoscale flows induced by vegetation or soil moisture inhomogeneities (Mahfouf et al. 1987a; Pinty et al. 1989), downslope windstorms (Richard et al. 1989), mountain waves (Nickerson et al. 1986; Richard et al. 1985; Romero et al. 1995), or the breeze circulation (in Florida, Mahfouf et al. 1987b; in Mallorca, Ramis and Romero 1995).

The primitive-equation model is hydrostatic and was initially described by Nickerson and Magaziner (1976). A more complet version is presented in Nickerson et al. (1986). Model equations are expressed in a terrain-following coordinate system (see Fig. 2.1), where the vertical coordinate ν is related to the classical σ pressure coordinate ($\sigma = (P - P_t)/(P_s - P_t) = (P - P_t)/\pi$) by the expression

$$\sigma = (4\nu - \nu^4)/3,$$

where ν and σ take values from 0 (upper boundary of pressure Pt) to 1 (ground). The vertical coordinate also satisfies the condition that $d\sigma/d\nu$ must be finite over the entire domain and must be equal to zero at the lower boundary to assure second order accuracy in the discretization scheme (De Rivas 1972). Terrain-following coordinates are very convenient in domains with complex terrain. They facilitate the treatment of the lower boundary since the ground is a surface of constant vertical coordinate. In particular, the ν coordinate has the advantage of allowing for a high resolution of the PBL in spite of working with an uniform grid.

The governing equations and physical parameterizations are presented in next sections (see Appendix 1 for symbols). Although the simulations are two-dimensional, the three-dimensional version of the model is presented. The model becomes automatically two-dimensional by eliminating all derivatives in the y-direction and the Coriolis force in the motion equations ($f \to 0$).

2.1 Dynamical equations

The prognostic equations for the horizontal momentum variables (u,v) have the form:

$$\frac{\partial \pi u}{\partial t} = -\frac{\partial \pi u u}{\partial x} - \frac{\partial \pi u v}{\partial y} - \frac{1}{\sigma'}\frac{\partial \sigma' \pi u \dot{\nu}}{\partial \nu} + f\pi v + \left(\phi - \frac{R_v T^* \sigma \pi}{P}\right)\frac{\partial \pi}{\partial x} - \frac{\partial \pi \phi}{\partial x} + F_{\pi u} + D_{\pi u} \quad (2.1)$$

$$\frac{\partial \pi v}{\partial t} = -\frac{\partial \pi v u}{\partial x} - \frac{\partial \pi v v}{\partial y} - \frac{1}{\sigma'}\frac{\partial \sigma' \pi v \dot{\nu}}{\partial \nu} - f\pi u + \left(\phi - \frac{R_v T^* \sigma \pi}{P}\right)\frac{\partial \pi}{\partial y} - \frac{\partial \pi \phi}{\partial y} + F_{\pi v} + D_{\pi v}. \quad (2.2)$$

In the (x, y, ν) coordinates the continuity equation is written

$$\frac{\partial \pi}{\partial t} = -\frac{\partial \pi u}{\partial x} - \frac{\partial \pi v}{\partial y} - \frac{1}{\sigma'}\frac{\partial \sigma' \pi \dot{\nu}}{\partial \nu}.$$

Since the boundary conditions on the vertical velocity $\dot{\nu}$ are:

1. At the surface: $\dot{\nu} = 0$ (the flow must be along the surface, i.e normal component zero).
2. Top of the domain: $\dot{\nu} = 0$ (this is a reasonable condition when the pressure at the upper boundary P_t is not greater than 100 hPa).

then the continuity equation can be vertically integrated over part of the atmosphere to give the vertical velocity $\dot{\nu}$:

$$\dot{\nu} = -\frac{1}{\pi \sigma'}\int_0^{\nu} \sigma' \left(\frac{\partial \pi}{\partial t} + \frac{\partial \pi u}{\partial x} + \frac{\partial \pi v}{\partial y}\right) d\nu, \quad (2.3)$$

or over the entire atmosphere to give the temporal evolution of the surface pressure:

$$\frac{\partial \pi}{\partial t} = -\int_0^1 \left(\frac{\partial \pi u}{\partial x} + \frac{\partial \pi v}{\partial y}\right) \sigma' \, d\nu. \quad (2.4)$$

Finally, the geopotential ϕ is calculated from the hydrostatic equation:

$$\frac{\partial \phi}{\partial \hat{P}} = -C_p \theta (1 + 0.61 q_v). \quad (2.5)$$

2.2 Thermodynamical equations

An entropy variable $S = \pi H$ is defined, where

$$H = \ln\left(\frac{T}{\hat{P}}\right) + \frac{L_v q_v}{C_p T}$$

apart from a small correction factor which is proportional to the mixing ratio of liquid water present in the model, is conserved during both dry and wet reversible adiabatic transformations (Dufour and Van Mieghem 1975). The present case consists of an open system in which the condensation products do not necessarily remain in the air if precipitation forms. However, the entropy variable is aproximately conserved in this pseudoadiabatic, pseudoreversible system. Its predictive equation is:

$$\frac{\partial S}{\partial t} = -\frac{\partial S u}{\partial x} - \frac{\partial S v}{\partial y} - \frac{1}{\sigma'}\frac{\partial \sigma' S \dot{\nu}}{\partial \nu} + F_S + D_S + S_S. \quad (2.6)$$

The other predicted thermodynamic variable is the moisture variable $W = \pi(q_v + q_{cw})$, in which transformation between mixing ratios of water vapour q_v and cloud water q_{cw} when saturation occurs is taken into account:

$$\frac{\partial W}{\partial t} = -\frac{\partial W u}{\partial x} - \frac{\partial W v}{\partial y} - \frac{1}{\sigma'}\frac{\partial \sigma' W \dot{\nu}}{\partial \nu} + F_W + D_W + S_W. \tag{2.7}$$

The source-sink terms S_S and S_W in Eqs. 2.6 and 2.7 will contain, respectively, radiative processes (short and long wave), and transformations between rainwater and the moisture variable W (loss by autoconversion and accretion, and production by evaporation). Parameterizations of these processes are explained in section 2.3 and 2.6.

Temperature and cloud water mixing ratio are not explicitly predicted by the model, but are diagnosed from the predicted values of S and W (Nickerson 1979). If the air is saturated, the mixing ratio is a known function of temperature, and the definition of S becomes a transcendental equation for the temperature T_s, corresponding to saturation with respect to liquid water. Excess vapour from the saturation value is converted into cloud water. If on the other hand the air is unsaturated, cloud water is zero, the vapour mixing ratio in the definition of S is replaced by W/π and the temperature is solved for directly, using the temperature at the previous time step to account for the temperature dependence of the latent heat.

In summary, T_s and q_{vs}, the saturation temperature and its corresponding vapour mixing ratio, are computed from the value of S using the Newton-Raphsonn technique. Temperature and mixing ratios of water vapour and cloud water are then arrived at in accordance with the following criteria:

$$\left.\begin{array}{rcl} q_v &=& q_{vs} \\ q_{cw} &=& W/\pi - q_{vs} \\ T &=& T_s \end{array}\right\} W > \pi q_{vs}$$

$$\left.\begin{array}{rcl} q_v &=& W/\pi \\ q_{cw} &=& 0 \\ T &=& T_{uns} \end{array}\right\} W \leq \pi q_{vs}$$

The saturation vapor pressure with respect to water, e_s, used to compute q_{vs}, is taken from Murray (1967):

$$e_s = 6.11 \exp[17.27(T - 273.16)/(T - 35.86)].$$

2.3 Microphysical equations

Apart from cloud water which wafts around with the air, liquid water in the model is present as rainwater, which falls through the air. Ice processes are not considered. Separate prognostic equations are written for both rainwater mixing ratio q_r and number of raindrops concentration N_r:

$$\frac{\partial \pi q_r}{\partial t} = -\frac{\partial \pi q_r u}{\partial x} - \frac{\partial \pi q_r v}{\partial y} - \frac{1}{\sigma'}\frac{\partial \sigma' \pi q_r \dot{\nu}}{\partial \nu} + F_{\pi q_r} + D_{\pi q_r} + S_{\pi q_r} \tag{2.8}$$

$$\frac{\partial \pi N_r}{\partial t} = -\frac{\partial \pi N_r u}{\partial x} - \frac{\partial \pi N_r v}{\partial y} - \frac{1}{\sigma'}\frac{\partial \sigma' \pi N_r \dot{\nu}}{\partial \nu} + F_{\pi N_r} + D_{\pi N_r} + S_{\pi N_r}. \tag{2.9}$$

The terms $S_{\pi q_r}$ and $S_{\pi N_r}$ are related to autoconversion, selfcollection, accretion, evaporation and sedimentation processes. However, selfcollection affects only the concentration of raindrops whereas accretion affects only the rainwater mixing ratio:

$$S_{\pi q_r} = \pi \left.\frac{\partial q_r}{\partial t}\right|_{auto} + \pi \left.\frac{\partial q_r}{\partial t}\right|_{accr} + \pi \left.\frac{\partial q_r}{\partial t}\right|_{eva} + \pi \left.\frac{\partial q_r}{\partial t}\right|_{sed} \tag{2.10}$$

$$S_{\pi N_r} = \pi \left.\frac{\partial N_r}{\partial t}\right|_{auto} + \pi \left.\frac{\partial N_r}{\partial t}\right|_{self} + \pi \left.\frac{\partial N_r}{\partial t}\right|_{eva} + \pi \left.\frac{\partial N_r}{\partial t}\right|_{sed}. \tag{2.11}$$

Diffusional growth of raindrops is not included since the model does not permit supersaturation with respect to water. The parameterization of the above terms is based on the assumption that rainwater is lognormally distributed with diameter; that is,

$$dN_r = \frac{N_r}{(2\pi)^{1/2}\sigma_0 D} \exp\left[-\frac{1}{2\sigma_0^2}\ln^2\left(\frac{D}{D_0}\right)\right] dD \tag{2.12}$$

is the number of raindrops in the size range D to $D + dD$ and N_r is the total number of raindrops. Here σ_0 and D_0 are distribution parameters. The lognormal distribution adequately describes the average spectra for a number of rainfalls of several intensities (Markowitz 1976).

If the diameter D_0 is large enough so that cloud-size droplets contribute very little to the total number concentration, the integration of Eq. 2.12 over the entire spectrum of drops of mass $\pi\rho_l D^3/6$ yields the following expression for q_r, the rainwater mixing ratio:

$$q_r = \frac{N_r}{\rho}\left(\frac{\pi}{6}D_0^3\rho_l\right)\exp\left(\frac{9}{2}\sigma_0^2\right),$$

where ρ and ρ_l represent the density of air and liquid water respectively. It is also convenient to define a mean drop diameter $\bar{D}_r$, which is the diameter the raindrops would have if they were all the same size. $\bar{D}_r$ is related to the lognormal distribution parameters by

$$\bar{D}_r = D_0 \exp\left(\frac{3}{2}\sigma_0^2\right).$$

Since there are two independent distribution parameters σ_0 and D_0, only one of which can be diagnosed given q_r and N_r, the microphysical system of equations is closed by assuming a constant value for σ_0 ($= 0.547$) and computing $\bar{D}_r$.

A detailed derivation of each contribution in Eqs. 2.10 and 2.11 making extensive use of the work of Berry and Reinhardt (1973), can be found in Nickerson et al. (1986). Only the final expressions (in mks units) to parameterize each source-sink term will be given in this summary.

a. Autoconversion

Autoconversion is the growth of cloud water to form rainwater. The tendency for rainwater mixing ratio is given by

$$\left.\frac{\partial q_r}{\partial t}\right|_{auto} = \alpha \rho q_{cw}^2,$$

and the corresponding expression for the number concentration of raindrops is

$$\left.\frac{\partial N_r}{\partial t}\right|_{auto} = 3.5 \times 10^9 \rho \left.\frac{\partial q_r}{\partial t}\right|_{auto},$$

where

$$\alpha = 0.067\{10^{16} x_{fcw}^{4/3} (varx)^{1/2} - 2.7\} \times \{10^4 [x_{fcw} (varx)^{1/2}]^{1/3} - 1.2\}.$$

In the expresion for α, x_{fcw} is the mean mass of the cloud droplets and $varx$ is a variance parameter. Both are related to the size distribution of the cloud water. It is assumed that the cloud droplets are also partitioned according to a lognormal distribution for which the distribution parameters σ_{0cw} and D_{0cw} remain constant.

$$varx = \exp(9\sigma_{0cw}^2) - 1$$

$$x_{fcw} = \frac{\rho q_{cw}}{N_{cw}} = \pi \rho_l \bar{D}_{cw}^3 / 6,$$

where the mean diameter of the cloud droplets $\bar{D}_{cw}$ is

$$\bar{D}_{cw} = D_{0cw} \exp\left(\frac{3}{2}\sigma_{0cw}^2\right).$$

The chosen values $D_{0cw} = 32.5\mu$m and $\sigma_{0cw} = 0.2203$ lead to a value of $\alpha = 4$.

b. Accretion

Accretion is the process whereby cloud droplets are collected by raindrops. Obviously, this process affects the rainwater mixing ratio but not the number of raindrops concentration:

$$\left.\frac{\partial q_r}{\partial t}\right|_{accr} = \frac{3\rho q_r q_{cw}}{2\rho_l D_{gr}} \gamma_c^2(D_{gr}, \bar{D}_{cw})[\upsilon(D_{gr}) - \upsilon(\bar{D}_{cw})],$$

where D_{gr} is the diameter corresponding to the predominant mass relative to the rainwater spectrum,

$$D_{gr} = \left(\frac{6\rho q_r}{\pi \rho_l N_r}\right)^{1/3} \exp(3\sigma_0^2).$$

For evaluation of the collision efficiency γ_c, the following aproximation based on Berry (1967) and Shafrir and Neiburger (1963) is adopted:

$$\gamma_c(r_l, p) = 1 + p + \frac{d}{p^f} + \frac{e}{(1-p)^g},$$

where $p = r_s/r_l$ is the ratio of the radius of the small drop to the radius of the collector drop, and

$$d = -27/r_l^{1.65}$$

$$e = -58/r_l^{1.9}$$

$$f = (15/r_l)^4 + 1.13$$

$$g = (16.7/r_l)^8 + 0.004r_l + 1.$$

with the radii expressed in micrometers.

Berry and Pranger (1974) have developed an empirical expression for the terminal velocity of the form

$$\upsilon(D) = \frac{\eta Re}{D\rho}, \tag{2.13}$$

where Re is the Reynolds number for the airflow around the drops, and η, the dynamic viscosity of the air, is given by the relation

$$\eta = 1.496286 \times 10^{-6} \frac{T^{1.5}}{T + 120}.$$

The expressions for Reynolds number are based on the data of Beard and Pruppacher (1969) and Gunn and Kinzer (1949):

$$Re = \begin{cases} 0.0412657y - 1.50074 \times 10^{-4}y^2 \\ +7.58884 \times 10^{-7}y^3 - 1.68841 \times 10^{-9}y^4 & \text{when } 0 < y \leq 175.27 \\ \\ \exp[-2.36534 + 0.767787 \ln y \\ +0.00535826(\ln y)^2 - 7.63554 \times 10^{-4}(\ln y)^3] & \text{when } 175.27 < y \leq 10^7 \end{cases}$$

The parameter y is given by

$$y = \frac{4\rho\rho_l g}{3\eta^2} D^3.$$

c. Selfcollection

Selfcollection is the process by which collisions between raindrops produce larger drops. In contrast to the growth by accretion, the interacting drops are of the same size range. The expression is

$$\left.\frac{\partial N_r}{\partial t}\right|_{self} = -b_s(\tilde{D}, D^*) N_r \rho q_r,$$

where

$$b_s(D, D') = \frac{3D^2}{2\rho_l(D^3 + D'^3)} \gamma_c^2(D, D')[\upsilon(D) - \upsilon(D')].$$

In the parameterization $\tilde{D} = D_{gr}$ and $D^* = \bar{D}_r$, already defined.

d. Sedimentation

Sedimentation of N_r and q_r is given by the divergence of their fluxes (driven by the terminal fall velocity), through a unit horizontal surface:

$$\left.\frac{\partial N_r}{\partial t}\right|_{sed} = \frac{\partial S_n}{\partial z}$$

$$\left.\frac{\partial q_r}{\partial t}\right|_{sed} = \frac{\partial S_q}{\partial z}.$$

The fluxes are calculated as

$$S_n = \frac{N_r \upsilon(D_0)}{2^{1/2}\sigma_0 p} \exp\left[\frac{(k_2-1)^2}{4p^2}\right]$$

$$S_q = \frac{q_0 \upsilon(D_0)}{2^{1/2}\sigma_0 p} \exp\left[\frac{(k_2+2)^2}{4p^2}\right].$$

For the calculation of the terminal fall velocity in terms of Reynolds number and dynamic viscosity as expressed in 2.13, Berry and Pranger (1974) give the following expression for the Reynolds number:

$$Re(D) = \exp[c1 + c2(\ln y) + c3(\ln y)^2].$$

The constants $c1$, $c2$ and $c3$ take the values -3.12611, 1.01338 and -0.0191182 respectively, and

$$y = \left(\frac{4\rho\rho_l g}{3\eta^2}\right) D^3 = aD^3.$$

The other constants which appear in the expressions of S_n and S_q are given by

$$p^2 = \left(\frac{1}{2\sigma_0^2} - 9c_3\right)$$

$$k_2 = 3c_2 + 6c_3 \ln(aD_0^3)$$

$$q_0 = \frac{N_r m(D_0)}{\rho}.$$

e. Rain evaporation

The evaporation rate of rainfall is given by the expression

$$\left.\frac{\partial q_r}{\partial t}\right|_{eva} = \frac{\rho_l}{\rho}\frac{\pi}{2} A S N_r \left[0.572 D_O \exp\left(\frac{\sigma_0^2}{2}\right) + 5.31\times 10^3 D_O^2 \exp(2\sigma_0^2) - 4.33\times 10^5 D_O^3 \exp\left(\frac{9\sigma_0^2}{2}\right)\right]$$

which combines the ventilation effect, the undersaturation S given by the expression

$$S = \frac{q_v}{q_{vs} - 1},$$

and A, a thermodynamical function of pressure and temperature:

$$A = \frac{1}{1000(d1 + d2)}.$$

The parameters $d1$ and $d2$ are calculated with the expressions:

$$d1 = \frac{R_v T P}{2.26 e_s \left(\frac{T}{T_0}\right)^{1.81}}$$

and

$$d2 = \frac{L_v}{T(0.0243 + 8 \times 10^{15}(T - T_0))} \left(\frac{L_v}{R_v T} - 1\right).$$

Finally, the number of raindrops which completely evaporate during one model time step is given by

$$N_{r_{eva}} = \frac{1}{\Delta t} \int_0^{D_{crit}} \frac{N_r}{(2\pi)^{1/2} \sigma_0 D} \exp\left(-\frac{1}{2\sigma_0^2} \ln^2 \frac{D}{D_0}\right) dD,$$

where

$$D_{crit} = (-2AS\Delta t)^{1/2}.$$

2.4 Diffusion terms and TKE equation

In the model equations 2.1, 2.2, 2.6, 2.7, 2.8, 2.9 and 2.15, the terms noted as D_{var} ($var = \pi u$, πv, S, W, πq_r, πN_r, πe) represent the horizontal diffusion, which acts on the ν-surfaces and is numerically introduced by a fourth order operator $D_4(var)$:

$$D_4(var) = K_H \left[\frac{\partial^4(var)}{\partial x^4} + \frac{\partial^4(var)}{\partial y^4}\right],$$

where K_H is a constant coefficient.

The fourth order diffusion is more selective than the second order one, and therefore eliminates effectively short wavelength contributions that can lead to nonlinear instability (Pielke 1984, chapter 10), whereas preserves the meteorological modes of longer wavelengths much better. Table 2.1 illustrates the different behaviour of second and fourth order diffusion, and shows the convenience of using the fourth order representation for the horizontal diffusion.

On the other hand, the F_{var} terms of the governing equations represent the vertical turbulent mixing. They are parameterized according to an eddy coefficient K_{ex}:

$$F_{var} = B \frac{\partial}{\partial \nu} \left(B K_{ex} \frac{\partial var}{\partial \nu}\right), \tag{2.14}$$

where

$$B = -\frac{gP}{\pi R_v T \sigma'}.$$

The exchange coefficients K_{ex} (K_m for the momentum, K_θ for the thermodynamic and microphysical variables and K_e for the mean turbulent kinetic energy TKE), are calculated as functions of the TKE (one and a half order closure) and the mixing length l_k following Therry and Lacarrère (1983) and Bougeault and Lacarrère (1989):

$$K_m = C_k l_k e^{1/2}$$

$$K_\theta = \alpha_T K_m$$

$$K_e = \alpha_e K_m.$$

The TKE (e) is predicted by the model through the equation:

$$\begin{aligned}\frac{\partial \pi e}{\partial t} &= -\frac{\partial \pi e u}{\partial x} - \frac{\partial \pi e v}{\partial y} - \frac{1}{\sigma'}\frac{\partial \sigma' \pi e \dot{\nu}}{\partial \nu} + \pi K_m \left[\left(B\frac{\partial u}{\partial \nu}\right)^2 + \left(B\frac{\partial v}{\partial \nu}\right)^2\right] - \\ &\frac{g}{\theta_v}\pi K_\theta B\left(\frac{\partial \theta_v}{\partial \nu} - \gamma_{cg}\right) - C_\epsilon \pi \frac{e^{3/2}}{l_\epsilon} + F_{\pi e} + D_{\pi e}, \qquad (2.15)\end{aligned}$$

where the first, second and third terms on the right-hand side are the advective terms, the fourth term is the shear-production term, the fifth is the bouyancy term and the sixth term represents the turbulence dissipation. The constant γ_{cg} is the so-called "countergradient" correction (Deardorff 1972), which applies only in the convective PBL, and allows for slightly stable stratification persinting with upward heat flux.

In the above relations, the inverse turbulent Prandtl numbers α_T and α_e are given the values $\alpha_T = \alpha_e = 1$. The numerical coefficients C_k and C_ϵ, once ajusted to experimentally determined values, take the values $C_k = 0.4$ and $C_\epsilon = 1/1.4$ (Bougeault and Lacarrère 1989).

Generalized specifications for the mixing length l_k and the dissipation length l_ϵ, based on the resistance to vertical displacements due to the static stability, are used by the model following Bougeault and Lacarrère (1989). This parameterization gives a good response outside the PBL and therefore is appropiate for orography-induced turbulence.

$$l_k = \min(l_{up}, l_{down})$$

$$l_\epsilon = (l_{up} l_{down})^{1/2}.$$

For each level Z in the atmosphere, l_{up} and l_{down} are the distances that a parcel originating from this level, and having an initial kinetic energy equal to the mean TKE of the layer, can travel upward and downward respectively, before being stopped by buoyancy effects. More precisely, l_{up} and l_{down} are defined by

$$\int_Z^{Z+l_{up}} \beta(\theta(Z) - \theta(Z'))\, dZ' = e(Z)$$

$$\int_{Z-l_{down}}^{Z} \beta(\theta(Z') - \theta(Z))\, dZ' = e(Z),$$

where β is the buoyancy coefficient ($\beta = g/T$).

2.5 Surface submodel

To apply the equation 2.14, which contains the expression for the vertical turbulent diffusion F_{var} in the boundary layer, it is necessary to know the turbulent fluxes $BK_{ex}\frac{\partial var}{\partial \nu}$ at the lower boundary ($\nu = \sigma = 1$). These are given by

$$BK_m \frac{\partial \pi u}{\partial \nu} = \pi Q_m \cos\alpha$$

$$BK_m \frac{\partial \pi v}{\partial \nu} = \pi Q_m \sin\alpha$$

$$BK_\theta \frac{\partial S}{\partial \nu} = \pi \left(\frac{Q_s \hat{P}}{T} + \frac{L_v Q_e}{C_p T} \right)$$

$$BK_\theta \frac{\partial W}{\partial \nu} = \pi Q_e,$$

where $\tan\alpha = V_h/U_h$, the ratio of the two wind components at the first grid point above the surface, and where Q_m, Q_s and Q_e represent the vertical eddy fluxes of momentum, sensible heat and water vapour at the surface:

$$Q_m = u_*^2$$

$$Q_s = -u_* \theta_*$$

$$Q_e = -u_* q_*,$$

where u_*, θ_* and q_* are scaling velocity, temperature and specific humidity.

The above turbulents fluxes are calculated in the model following the surface layer parameterization of Louis (1979). The scheme is based on the Monin-Obukhov similarity theory with bulk relations evaluated between the surface, with roughness length z_0, and the lowest model level at a height z above the ground. In summary, defining the bulk Richardson number (a stability parameter) for the layer

$$Ri_B = \frac{gz\Delta\theta}{\bar{\theta}u^2},$$

the surface eddy fluxes are calculated as

$$u_*^2 = a^2 u^2 F_m \left(\frac{z}{z_0}, Ri_B \right)$$

$$u_* \theta_* = \frac{a^2}{R} u \Delta\theta F_h \left(\frac{z}{z_0}, Ri_B \right)$$

$$u_* q_* = \frac{a^2}{R} u \Delta q F_h \left(\frac{z}{z_0}, Ri_B \right),$$

where

$$a^2 = k^2 \Big/ \left(\ln \frac{z}{z_0} \right)$$

is the drag coefficient in neutral conditions (k is the Von Karman constant), and u refers here to the total wind, not to the x-component. The constant R, ratio of the drag coefficients for momentum and heat in the neutral limit, was estimated by Businger et al. (1971) to be 0.74. The universal functions F_m and F_h are adjusted for each of the following regimes:

1. In the unstable case ($Ri_B \leq 0$):

$$F = 1 - \frac{bRi_B}{1 + c|Ri_B|^{1/2}}.$$

2. In stable conditions ($Ri_B > 0$):

$$F = 1/(1 + b'Ri_B)^2,$$

where the factors b, b' and c are given by

$$b = 2b' = 9.4$$

$$c = C^* a^2 b \left(\frac{z}{z_0}\right)^{1/2}.$$

$C^* = 7.4$ for momentum and 5.3 for the heat and moisture fluxes.

3. For free convection ($u \to 0$ and $Ri_B < 0$):

$$u_* \theta_* = -\frac{1}{5.3R_v} \left(\frac{gz_0}{\bar{\theta}}\right)^{1/2} \Delta\theta^{3/2}$$

$$u_* q_* = -\frac{1}{5.3R_v} \left(\frac{gz_0}{\bar{\theta}}\right)^{1/2} \Delta\theta^{1/2} \Delta q.$$

4. In the case $u \to 0$ and $Ri_B \geq 0$:

$$u_* \theta_* = u_* q_* = 0.$$

As can be seen in the above expressions, the surface eddy fluxes are directly dependent on the surface values of temperature and humidity. In particular, the necessary θ_{z_0} and q_{z_0} are calculated from the surface values θ_G and q_G with the expressions

$$\theta_{z_0} = \theta_G + 0.0962(\theta_*/k)(u_* z_0/\nu)^{0.45}$$

$$q_{z_0} = q_G + 0.0962(q_*/k)(u_* z_0/\nu)^{0.45},$$

where ν the kinematic viscosity of air.

Except over water masses as seas or lakes, where the surface temperature is assumed constant and the humidity is saturant, these parameters can vary significantly during the diurnal cycle. As a consequence, the surface sub-model is closed solving the energy and water budget equations at the air-soil interface to obtain the temperature and moisture at the surface. Difussion equations for temperature and moisture content are solved in the

soil, which is divided into several vertical levels. Such balances are significantly affected by the presence of vegetation, which modifies the partition and intensity of the surface turbulent fluxes. Its effect is modulated through the shielding factor, defined as the fractional coverage on a grid area by a dense vegetation canopy.

For convenience, we distinguish between bare soil and vegetative surfaces. Only the main formulations applied by the surface sub-model are given. For more details and for a description of the numerical implementation of the scheme, see Mahfouf et al. (1987a), Pinty et al. (1989), McCumber and Pielke (1981) and Deardorff (1978).

a. Bare soil

The land surface temperature $(T_s)_G$ for a surface of emissivity ϵ and albedo α, is computed by a iterative solution to the energy balance equation

$$(1-\alpha)R_S + \epsilon R_L - \epsilon\sigma(T_s)_G^4 + \rho L_v u_* q_* + \rho C_p u_* \theta_* - (H_s)_G = 0. \tag{2.16}$$

R_S and R_L in the first and second terms are the solar and downcoming longwave radiative fluxes respectively, and the third term the outgoing longwave radiation from the surface (σ is the Stefan-Boltzman constant). Therefore, the three terms combined form the net radiation at the surface. The fourth, fifth and sixth terms are the latent, sensible and soil heat fluxes.

On the other hand, the moisture at the surface is obtained by solving the water budget equation

$$\rho u_* q_* + P - (W_s)_G = 0,$$

where P is the precipitation rate and $(W_s)_G$ the soil moisture flux at the surface.

The ground heat flux, H_s, and soil moisture flux, W_s, are written as

$$H_s = -\lambda \frac{\partial T_s}{\partial Z}$$

$$W_s = -\rho_w K_\eta \frac{(\psi + Z)}{\partial Z},$$

where ρ_w is the liquid water density, ψ the moisture potential, K_η the hydraulic conductivity of the soil and λ its thermal conductivity.

These fluxes are obtained by solving for several levels in the first meter of soil, diffusion equations for the temperature, T_s, and the volumetric moisture content, η:

$$\rho c \frac{\partial T_s}{\partial t} = \frac{\partial}{\partial Z}\left(\lambda \frac{\partial T_s}{\partial Z}\right)$$

$$\frac{\partial \eta}{\partial t} = \frac{\partial}{\partial Z}\left(D_\eta \frac{\partial \eta}{\partial Z}\right) + \frac{\partial\ K_\eta}{\partial Z},$$

where ρc is the specific heat capacity of the soil and D_η its hydraulic diffusivity. A set of equations relate the variables ψ, K_η, D_η, ρc and λ as functions of the soil moisture:

$$\psi = \psi_s \left(\frac{\eta_s}{\eta}\right)^b$$

$$K_\eta = K_{\eta_s}\left(\frac{\eta}{\eta_s}\right)^{2b+3}$$

$$D_\eta = -\frac{bK_{\eta_s}\psi_s}{\eta}\left(\frac{\eta}{\eta_s}\right)^{b+3}$$

$$\rho c = (1-\eta_s)\rho_i c_i + \eta\rho_w c_w$$

$$\lambda = 0.167\eta + 0.1.$$

In the above equations, the saturated values η_s, K_{η_s}, ψ_s, the volumetric heat capacity of dry soil $\rho_i c_i$, as well the exponent b, are functions of the soil texture. Here, $\rho_w c_w$ is the heat capacity of water.

The relative humidity at the surface is calculated as function of $(T_s)_G$ and the surface moisture potential ψ_G:

$$h = \exp\left(-\frac{g\psi_G}{R_v(T_s)_G}\right).$$

The surface specific humidity is then determined from

$$q_G = hq_s,$$

where q_s is the saturation value at the temperature $(T_s)_G$.

b. Vegetative surfaces

Based on Deardorff (1978), the surface scheme also allows for the inclusion of a single layer of vegetation which is assumed to have negligible heat capacity. A second energy budget is established for the foliage layer taking into account the exchanges above and below the canopy. The modified expressions for the sensible heat and the evapotranspiration fluxes (H_{sh} and E_h respectively) from the ground foliage system to the atmosphere are

$$H_{sh} = H_{sg} + H_{sf} = \rho C_p c_{Hg} u_{af}(T_g - T_{af}) + 1.1N\rho C_p c_f u_{af}(T_f - T_{af}), \tag{2.17}$$

$$E_h = E_g + E_f = \rho c_{Hg} u_{af}(q_g - q_{af}) + N\rho c_f u_{af}[q_{sat}(T_f) - q_{af}]r''. \tag{2.18}$$

The first term of the sensible heat flux (H_{sg})is the generalization of the sensible heat flux at the ground surface, and the second term (H_{sf}) the expression for the net sensible heat flux from the foliage to the surrounding air. Similarly, the first term of the evapotranspiration rate (E_g) denotes the evaporation at the ground surface, and the second term (E_f) the net foliage evaporation and/or transpiration rate per unit horizontal ground area.

In Eqs. 2.17 and 2.18, c_{Hg} is the heat and moisture transfer coefficient applicable to the ground surface underneath a canopy. It is given by interpolation between that aplicable to bare ground c_{H0}, and that applicable to the top of a dense canopy c_{Hh}:

$$c_{Hg} = (1-\sigma_f)c_{H0} + \sigma_f c_{Hh},$$

where σ_f represents the shielding factor.

T_g and T_f (and q_g and q_f), refer to ground surface and foliage surface values respectively. The mean properties of the air within the foliage, T_{af} and q_{af}, are assumed to be intermediate beween above-canopy air properties at $z = z_a$ (first atmospheric level of the model), foliage surface properties, and ground surface properties:

$$T_{af} = (1 - \sigma_f)T_a + \sigma_f(0.3T_a + 0.6T_f + 0.1T_g),$$

$$q_{af} = (1 - \sigma_f)q_a + \sigma_f(0.3q_a + 0.6q_f + 0.1q_g).$$

For the mean wind, the following expression is used

$$u_{af} = 0.83\sigma_f c_{Hh}^{1/2} u_a + (1 - \sigma_f)u_a.$$

The dimensionless heat transfer coefficient c_f which appears in Eqs. 2.17 and 2.18 is assumed to be given by

$$c_f = 0.01(1 + 0.3/u_{af}).$$

N, the net leaf area index, is defined as the total one-sided leaf area of the foliage relative to the ground area. As explained in Deardorff (1978), the fraction of potential evaporation from the foliage r'' is function of the liquid water retained on the foliage (predicted in response to precipitation and evaporation or condensation from or onto the leaves), the atmospheric resistance $(c_f u_{af})^{-1}$, and the stomatal resistance r_{st}, calculated with the expression

$$r_{st} = r_{st_{min}} S_{st} M_{st},$$

where $r_{st_{min}}$ is the minimum stomatal resistance (function of the vegetation type), S_{st} is the solar radiation factor and M_{st} is a factor limiting the transpiration when the soil becomes very dry or when the atmospheric demand is too strong (Pinty et al. 1989).

A gross energy budget for the foliage layer must be established in order to estimate T_f. The values at the top of the canopy being denoted by subscript h, those at the ground by subscript g, and the direction of radiative fluxes by arrows, the assumption of no canopy heat storage leads to

$$R_{Sh}\downarrow + R_{Lh}\downarrow - R_{Sh}\uparrow - R_{Lh}\uparrow - (R_{Sg}\downarrow + R_{Lg}\downarrow - R_{Sg}\uparrow - R_{Lg}\uparrow) = H_{sf} + L_v E_f,$$

where as in Eq. 2.16, R_S is the shortwave and R_L the longwave flux. The fluxes $R_{Sh}\downarrow$ and $R_{Lh}\downarrow$ are given by the radiation scheme. By definition of the shielding factor σ_f, $R_{Sg}\downarrow$ is given by

$$R_{Sg}\downarrow = (1 - \sigma_f)R_{Sh}\downarrow .$$

Given the ground albedo α_g, the reflected flux $R_{Sg}\uparrow$ is given by

$$R_{Sg}\uparrow = \alpha_g(1 - \sigma_f)R_{Sh}\downarrow .$$

The upward longwave flux just above the ground, $R_{Lg}\uparrow$, is obtained by interpolating with σ_f between the expression applicable above bare soil and that applicable just above soil overlain with a dense canopy:

$$R_{Lg}\uparrow = (1 - \sigma_f)[\epsilon_g \sigma T_g^4 + (1 - \epsilon_g)R_{Lh}\downarrow] + \sigma_f[\epsilon_g \sigma T_g^4 + (1 - \epsilon_g)\epsilon_f \sigma T_f^4]/(\epsilon_f + \epsilon_g - \epsilon_f \epsilon_g).$$

For $\sigma_f = 1$ this expression for $R_{Lg}\uparrow$ reverts to that for the radiative flux between two parallel surfaces of emissivities ϵ_g and ϵ_f. For $\sigma_f = 0$ the expression similarly accounts for the upward reflection of $R_{Lh}\downarrow$ from the ground when $\epsilon_g < 1$. The three remaining radiative fluxes are similarly obtained:

$$R_{Sh}\uparrow = \alpha_g(1-\sigma_f)R_{Sh}\downarrow + \alpha_f\sigma_f R_{Sh}\downarrow,$$

$$R_{Lh}\uparrow = (1-\sigma_f)[\epsilon_g\sigma T_g^4 + (1-\epsilon_g)R_{Lh}\downarrow] + \sigma_f[\epsilon_f\sigma T_f^4 + (1-\epsilon_f)R_{Lh}\downarrow],$$

$$R_{Lg}\downarrow = (1-\sigma_f)R_{Lh}\downarrow + \sigma_f[\epsilon_f\sigma T_f^4 + (1-\epsilon_f)\epsilon_g\sigma T_g^4]/(\epsilon_f + \epsilon_g - \epsilon_f\epsilon_g).$$

At the ground surface, the balance equations written for bare soil are mantained, but the fluxes are now represented by $R_{Sg}\downarrow$, $R_{Lg}\uparrow$, $R_{Lg}\downarrow$, H_{sg}, E_g, etc.

2.6 Radiation parameterization

Calculations of solar radiation R_S and downcoming longwave radiation R_L are necessary to solve the surface energy balances presented in section 2.5. The radiation scheme, based on Mahrer and Pielke (1977), determines the evolving radiative fluxes in the atmosphere. Therefore, it allows the calculation of R_S and R_L at the ground, and the solar radiative heating and longwave cooling rates for each atmospheric layer throgh the flux divergence. Both rates combine to give the source-sink term S_S in the thermodynamical equation 2.6.

Scattering and absorption of solar radiation by permanent gases such as oxygen, ozone and carbon dioxide is included in the scheme. Absorption and longwave emission by the atmospheric water constituents (water vapor and clouds) is also considered. For a detailed description of the radiation scheme, the reader can find the parameterized form of the shortwave transmissivity functions and longwave emissivities in Mahrer and Pielke (1977) and Pielke (1984, chapter 8). Only the formulation of the modified surface fluxes to account for the terrain slope is here given explicitaly:

Denoting $\bar{R}_S$ and $\bar{R}_L$ as the solar and longwave fluxes for a horizontal surface, for a slant surface the solar and infrared radiation will be modified to

$$R_S = \bar{R}_S \frac{\cos i}{\cos Z},$$

$$R_L = \bar{R}_L \cos\alpha.$$

The slope angle α is calculated from the terrain height z_G with the expression

$$\alpha = \tan^{-1}\left[\left(\frac{\partial z_G}{\partial x}\right)^2 + \left(\frac{\partial z_G}{\partial y}\right)^2\right]^{1/2}.$$

The solar zenith angle Z obeys $\cos Z = \sin\phi\sin\delta + \cos\phi\cos\delta\cos\psi$, where ϕ is the latitude, δ the solar declination and ψ the solar hour angle (see Fig. 2.2). Finally, i is the angle of incidence of solar rays on the inclined surface, where

$$\cos i = \cos\alpha\cos Z + \sin\alpha\sin Z\cos(\beta - \gamma).$$

Requiring that south has zero azimuth, the solar and slope azimuths β and γ are given by:

$$\beta = \sin^{-1}\left(\frac{\cos\delta \sin\psi}{\sin Z}\right),$$

$$\gamma = \tan^{-1}\left(\frac{\partial z_G}{\partial y} \Big/ \frac{\partial z_G}{\partial x}\right) - \frac{\pi}{2}.$$

2.7 Boundary conditions

At the top of the model domain, the vertical velocity $\dot{\nu}$ is set to zero. However, especially for the case of mountain waves, vertical transport of momentum may be very important and reach high altitudes, inducing reflection from the uppermost level with such boundary condition. To minimize reflection from the upper boundary, an absorbing layer containing several computational levels is included. In the absorbing layer, the background diffusion (imposed by a second order operator in this layer), is progresively increased, reaching its maximum value at the top level (Nickerson et al. 1986):

$$K_{H2} = K^*_{H2} + K^{abs}_{H2}\left(\sin\frac{\pi}{2}\frac{\sigma_{kabs} - \sigma_k}{\sigma_{kabs}}\right)^2 \text{ for } k < kabs.$$

In this expression, *kabs* is the number of vertical levels composing the absorbing layer. The second-order diffusion constant K_{H2} has the maximun value $K^*_{H2} + K^{abs}_{H2}$ at the top where $\sigma_1 = 0$, and equals the background value K^*_{H2} at level $k = kabs$

At the lateral boundaries, the values of the fields are prescribed externarlly. To avoid reflection, the prognostic variables are subjected to a forcing in the marginal zone (4 interior points from the boundary) that constrains them to relax towards the externally specified field on a time scale that varies with distance from the lateral boundary (Davies 1976).

2.8 Numerical aspects

For the integration of the governing equations, a staggered vertical grid (Fig. 2.3) is used. With reference to the figure, variable $\dot{\nu}$ is defined at the circled levels, and all other variables are defined at the crosses.

The horizontal grid (Fig. 2.4) is also staggered to reduce the truncation errors on the level ν surfaces (Anthes and Warner 1974). The dynamical variables u and v are defined at the crosses, while all thermodynamic variables are defined at the dots. The variable $\dot{\nu}$ is not defined on this horizontal level but at distances $\Delta\nu/2$ above or below this level and at positions corresponding to the dots.

Centered differences are used to represent the time and space derivatives (leapfrog scheme). That is, the terms of the equations are evaluated with centered spatial differences at the middle time level and used to advance the integration between $t - \Delta t$ and $t + \Delta t$ in a single step. However, for reasons of stability the horizontal diffusion term is evaluated at $t - \Delta t$. The vertical diffusion is treated implicitaly.

An Asselin filter is applied to connect odd and even time steps. The filtered value at the $t-1$ time level $\tilde{\chi}^{t-1}$ is given by

$$\tilde{\chi}^{t-1} = \chi^t + \alpha(\chi^{t+1} - 2\chi^t + \chi^{t-1}),$$

where the coefficient α takes a value of 0.25 (Schlesinger et al. 1983).

	$[K_H]$ (Second Order)					$[K_H]$ (Fourth Order)	
	0.25	0.10	0.05	0.01	0.001	-0.01	-0.001
$n = 2$	1	2	5	24	249	5	61
$n = 4$	1	4	9	49	499	24	249
$n = 6$	4	9	19	99	999	99	999
$n = 8$	6	17	33	170	1707	290	2913
$n = 10$	10	26	51	261	2618	684	6853
$n = 12$	14	37	74	373	3732	1392	13927
$n = 20$	40	102	203	1021	10215	10435	104363

Table 2.1. Number of time steps necessary to atenuate by e^{-1} a wave of wavelength $n\Delta x$ as function of the nondimensional diffusion coefficient $[K_H]$ for the second and fourth order diffusion operators (Richard et al. 1985). The nondimensional coefficients $[K_H]$ are defined as $K_H 2\Delta t/\Delta x^2$ and $K_H 2\Delta t/\Delta x^4$ for the second and fourth order respectively.

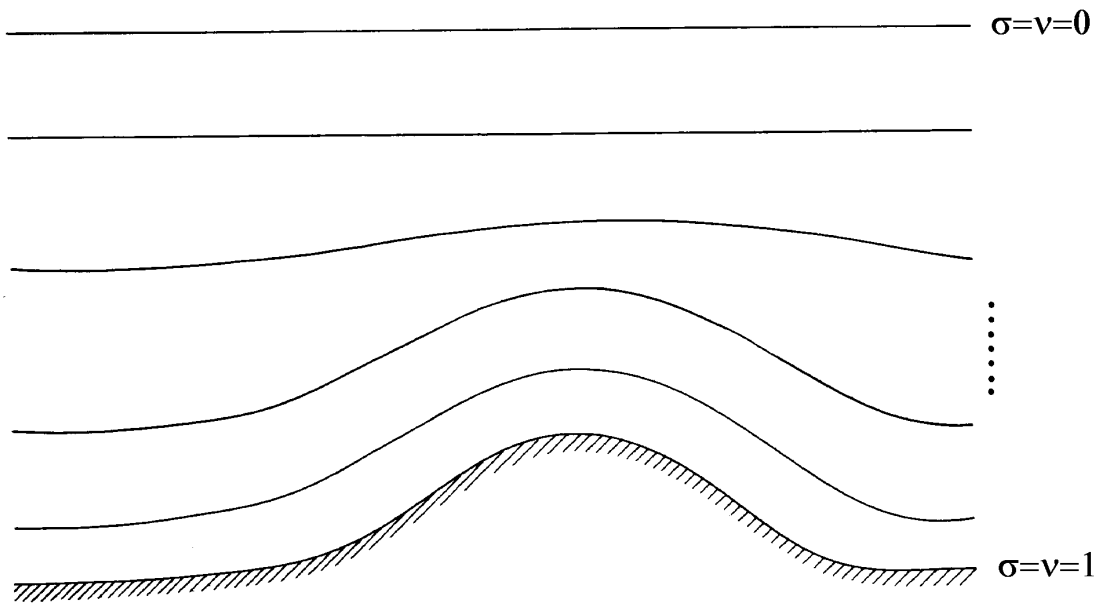

FIG. 2.1. Illustration of the terrain-following coordinate system.

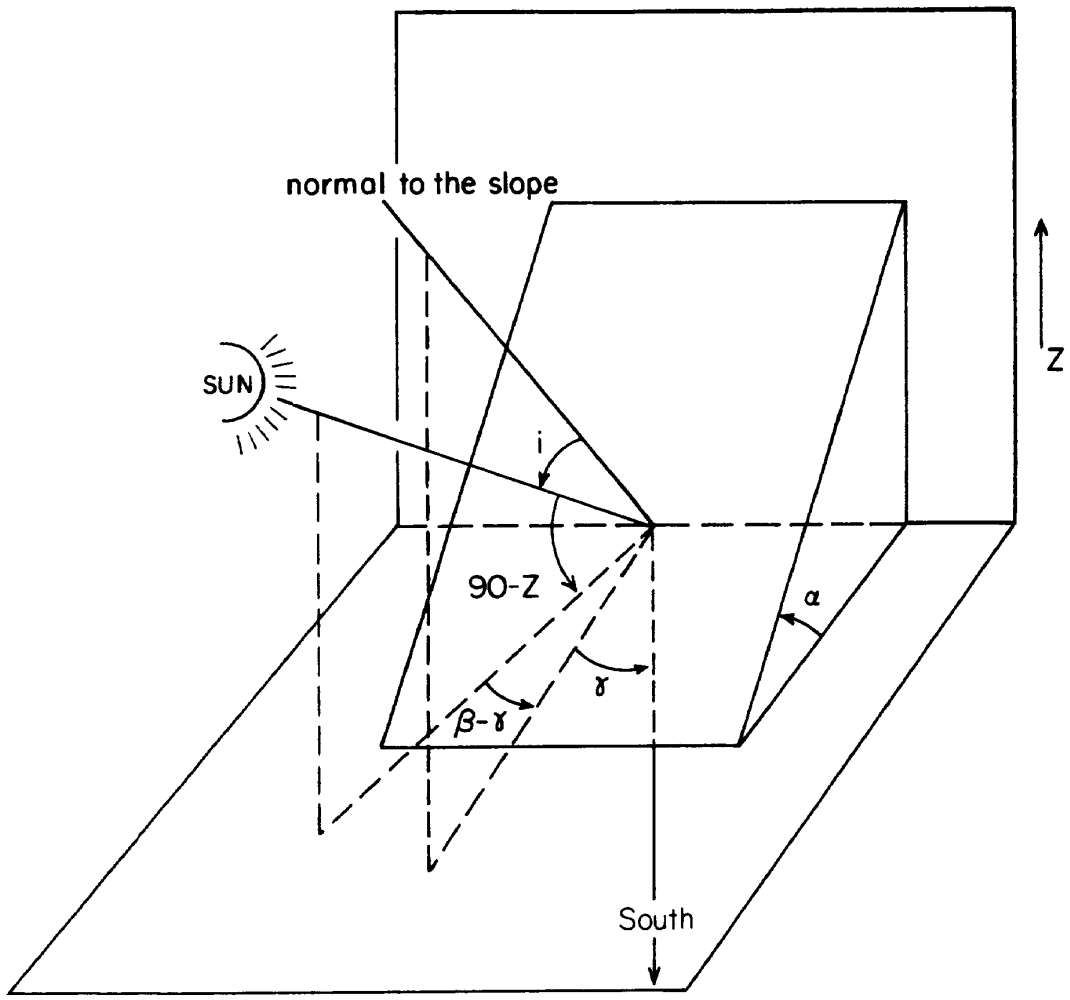

FIG. 2.2. Angles considered to derive the radiative fluxes for slant surfaces.

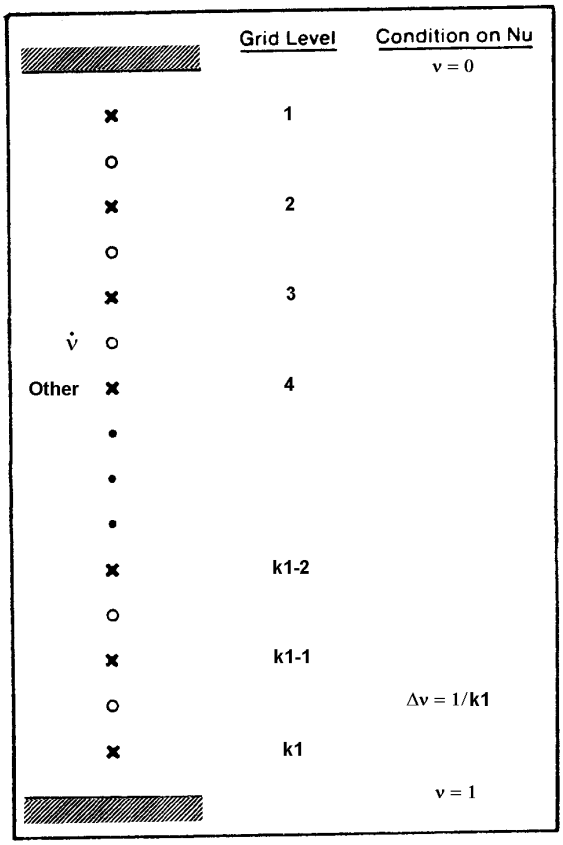

FIG. 2.3. Vertical grid of the numerical model.

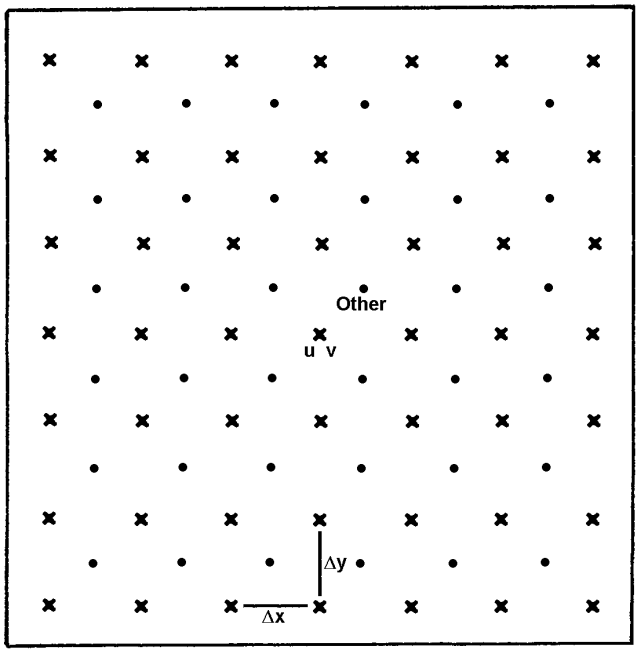

FIG. 2.4. Horizontal grid of the numerical model.

Chapter 3

RESULTS

3.1 Characteristics of the experiments

A set of four two-dimensional numerical experiments was carried out to study the influence of vegetation on the development and structure of the mountain wave, as well as on the distribution in time and space of surface parameters. The astronomical parameters for radiation calculations correspond to 21 March at a latitude of 40^0N. The simulations begin at 0600 LST (just after sunrise) and continue until 1800 LST (just before sunset). The model domain is 500 km in the W-E direction, with an horizontal grid length of 10 km. The time step is 10 seconds.

a. The atmosphere

As in previous works (Mahrer and Pielke 1978; Nickerson et al. 1986), the model is initialized with a single radio sounding, providing horizontally uniform initial fields. The layer below 300 hPa has a lapse rate of 6 K km^{-1} in which the temperature at zero elevation has a value of 280 K, and the layer between 300 hPa and the upper boundary (100 hPa) is isothermal. The wind is westerly with a vertically uniform speed of 20 m s^{-1}. Initially, the microphysical variables and all the surface fluxes are set to zero. Except for air moisture and surface characteristics, all the simulations are initialized in the same manner.

There are 15 ν vertical levels in the atmosphere between the top and botton boundaries. The vertical grid corresponding to the 15 levels is shown in Table 3.1, together with the corresponding σ levels. The resolution near the surface is significantly increased with the ν coordinate with respect to the usual σ coordinate. For the present cases, there are four computational levels in the lowest kilometer and the first one is 15 m above the ground aproximately.

Nondimensional values for second and fourth order diffusion coefficients are 0.01 and -0.01 respectively. The absorbing layer occupies the 5 upper levels of the domain, and the maximum diffusion induced at the top level has a nondimensional value of 0.10.

Using the method of Davies (1976), all the fields are relaxed toward their initial values at the lateral boundaries as has been done in previous works (e.g. Richard et al. 1989).

b. The surface

The orography consists of a north-south oriented ridge, centered in the domain and defined by the Agnesi function (Laprise and Peltier 1989):

$$z_s(x) = h/[1 + (x/a)^2]$$

where h and a are 1 km and 20 km respectively.

With the above values for h and a, we can calculate the representative nondimensional numbers Nh/U and Na/U for the flow considered. With the wind speed $U = 20$ m s^{-1} and the Brunt-Väisäla frequency N (not uniform in our case) given by its value at $z = h$, the nondimensional numbers result in $Nh/U \sim 0.8$ and $Na/U \sim 16$. These values confirm the nonlinear (without wave breaking) and hydrostatic nature of the mountain wave in study.

The soil, with a depth of 1 m, is divided into 13 vertical levels. A mixed soil type is used for all simulations. Its hydraulic, thermal and radiative properties are summarized in Table 3.2. For cases in which vegetation is included, two representative types of cover are considered, conifer forest and shrub. Their characteristics are listed in Table 3.3.

The experimental conditions are summarized in Table 3.4. Experiments 1 and 2 are carried out for bare soil but for different initial conditions of atmospheric moisture (dry atmosphere in Experiment 1 and a saturated atmosphere in Experiment 2), and are included for comparison with previous studies in which the surface energy budget was not used to calculate the surface temperature (Nickerson et al. 1986, Fig. 3.1).

In Experiments 3 and 4, both with saturated atmosphere, the surface is covered by vegetation. Two distinct vegetative regions are considered: the top ($z_s(x) \geq 500$ m) and the slopes ($z_s(x) < 500$ m). The shielding factor is homogeneous over each vegetation area.

For each of the four experiments, the temperature of the atmospheric sounding at the air-land interface was used to initialize the vertically uniform temperature within the soil. The volumetric water content of the soil was initially 60% of the saturated value.

3.2 Results and discussion

It is not the aim of this study to determine the effects of soil moisture and texture. Therefore, all the simulations presented in this work have been performed with the same soil properties.

3.2.1 Wave structure

The cross-sections presented correspond to the central part of the model domain. Two representative times are considered when discussing the results given by the model, 1200 LST and 1800 LST. The wave is represented by means of the potential temperature field. Because the potential temperature is nearly conserved along the trajectories of air

parcels, and because the patterns shown are quasi-stationary, the isopleths of potential temperature can be viewed as approximate streamlines of the airflow.

Figure 3.2 displays the wave obtained for Experiment 1. The maximum amplitude of the potential temperature wave develops at an altitude between 6 and 8 km over the lee of the ridge, and enhanced surface winds also appear in the lee. These results are qualitatively and quantitatively in agreement with previous experiments (Mahrer and Pielke 1978; Nickerson et al. 1986). However, in contrast to the conditions considered by Nickerson et al (1986), the surface temperature in our simulations is allowed to vary, thereby resulting in some differences, especially in the lower part of the atmosphere (compare Fig. 3.2 against Fig. 3.1a). The development of thermally induced slope winds could explain, for example, why in our experiment the west slope surface winds are stronger and the east slope winds weaker.

From Figures 3.2a and 3.2b, it can be also seen how the wave intensity decreases during the simulation. Without additional information, it is difficult to asses to what extent this result is a consequence of the diurnal variability in the boundary layer or if it is due to a spin up process within the model. This point will be discussed in section 3.2.5.

The saturated case (Experiment 2) after 12 hours of simulation is presented in Fig. 3.3a. In agreement with Durran and Klemp (1983), the figure shows that the inclusion of moisture produces a weaker wave than is obtained in the dry case. Comparing the result with Fig. 3.2b, it can be also seen that the inclination of the wave is smaller when moisture is present. The damping effects are the consequence of the reduction of the atmospheric stability in cloudy regions.

Another moisture effect derived from the heat released by the condensation products in the ascending slope is the additional warming in the lee (foehn effect). This moisture effect is detected from a comparison of Figs. 3.2b and 3.3a (see Fig. 3.3b for a detailed view). The same comparison shows that the lower atmosphere is warmer over the whole domain and less stable in the lee for the saturated case. This reduction of stability in the moist case was also present in the simulations of Nickerson et al. (1986) (see Fig. 3.1b).

Having established the validity of our results by comparison with previous works, two more experiments were carried out to study the effects of surface vegetation on the wave structure. Figures 3.4 and 3.5 display the results for Experiment 3 (non homogeneous vegetation) and Experiment 4 (homogeneous vegetation).

The wave obtained in case 3 (Fig. 3.4) is appreciably weaker than the wave with bare soil. The centers of maximum and minimum winds are situated 1 km higher in this case, and the mid tropospheric amplitude of the temperature wave is not as pronounced. Over the crest of the ridge where friction induced by conifers is very intense, the wind shear extends vertically to higher altitudes than in Experiment 2. At low levels, isotachs are more symmetrically distributed between both slopes in Fig. 3.4 than in Fig. 3.3a, indicating that a dense stand of tall trees at the crest of the mountain may significantly reduce the intensity of downslope winds. In this case, the wave intensity is also stronger at 1200 LST than at 1800 LST.

There is a region of reduced stability in the lower atmosphere over the eastern slope of the barrier at noon (Fig. 3.4a). Over that same area, the stratification becomes more stable by 1800 LST (Fig. 3.4b), but does not reach the degree of stability found over the western slope. Of all three saturated experiments, the reduction in lee side stability is

most pronounced in Experiment 3.

As expected, when the tall trees at the top of the mountain are replaced by shrub, the wave intensity given by the model (Fig. 3.5) evolves to an intermediate state between the results of Experiments 2 and 3. The reduced surface friction associated with the uniform covering of shrub on the slopes as well as on the crest of the mountain results in lee side surface winds that are 4 ms^{-1} stronger than when the crest is covered by tall trees.

3.2.2 Turbulent kinetic energy

An important aspect of the dynamical and thermodynamical fields induced by the mountain is the intensity and distribution or the turbulent kinetic energy. Figures 3.6 to 3.9 display the TKE obtained in the experiments, as well as the areas affected by clouds (no clouds are formed in case 1 since the moist soil is not a significant source of moisture for the atmosphere). In the prognostic equation of TKE (Eq. 2.15), in addition to the transport terms, there are three important terms which maintain a near balance in the free atmosphere, resulting in no net turbulence production. These are the shear production, the buoyancy production (negative in stable conditions), and the viscous dissipation. Wherever the stratification is sufficiently stable, even with appreciable wind shear, no turbulence appears. However, since in our experiments the stability of the PBL reaches low values, especially in the lee for the saturated cases as a result of the foehn effect, and since there are regions of strong wind shear close to the slopes, this leads to the generation of turbulence at low levels, primarily above the lee slope.

The TKE figures show that the turbulence is stronger at noon when the PBL is less stable than in the evening in all cases. However, the four simulations result in significant differences in the TKE intensity and distribution. We note in Figs. 3.6 to 3.9 that the dry case is not as favorable for turbulence production as the moist cases in spite of having stronger wind shear. This is because the midday reduction of the thermal stability only affects a very shallow layer close to the ground where the temperature increases markedly in response to the incoming solar radiation. In fact, the turbulence distribution in this case is very homogeneous along the domain at noon (Fig. 3.6a) since the increase of the surface temperature is nearly the same over the whole domain. Since the long wave radiation is not readily absorbed by the dry atmosphere, the surface cools rapidly during the afternoon, and by the end of the simulation, turbulence has practically disappeared except over the eastern slope where the wind shear is stronger (Fig. 3.6b).

In the saturated cases (Figs. 3.7 to 3.9), the solar radiation is appreciably absorbed and the ground temperature can not increase as much as will be seen in section 3.2.4. By way of contrast, downwind of the barrier the lower atmosphere remains slightly stable owing to the foehn warming effect. As a result, the turbulence distribution is highly skewed, with low values upwind of the barrier and high values downwind associated with the wind shear and light stability within the PBL.

It is important to note the role played by the conifer forest, through its extensive layer of wind shear, in the formation of a deep and intense turbulent layer (Fig. 3.8). That layer has a depth of 1 km in the lee of the mountain, but it also exists in a shallow layer above the western slope. The results for Experiments 2 and 4 (Figs. 3.7 and 3.9) are similar since there are only minor differences of wind and temperature at low levels. In

these cases, the region of turbulence is found in a shallow layer over the eastern slope.

3.2.3 Clouds and precipitation

The cloud water mixing ratio for the cases that were initially saturated is shown in Figs. 3.7, 3.8 and 3.9. The clouds induced by orographic uplifting over the upwind slope are present in all three experiments. The greatest vertical extent is observed for the case when the conifer forest covers the top of the mountain. The maximum values of the liquid water content are also obtained for this case (more than 0.25 gkg^{-1} close to the crest). The major differences between the three experiments upwind of the barrier is the strength of the cloud band at an altitude of 4 and 6 km. Cases 3 and 2 produce the highest and lowest liquid water concentrations respectively. Case 4 again produces intermediate values.

In addition, the vertical motion induced by the wave downwind of the barrier leads to the formation of a cloud with low liquid water content at an altitude between 6 and 8 km. Experiment 3 has the lowest liquid water content in that upper level cloud owing to a weaker intensity of the upper level wave. More condensation occurs in the upper level cloud of Experiment 4 (Fig. 3.9), but the greatest amount is produced in Experiment 2 (Fig. 3.7).

Model-predicted accumulated rainfall over the mountain barrier is shown in Fig. 3.10. The asymmetrical distribution of cloud water results in heavier rainfall over the upwind slope and crest, with an abrupt decrease over the lee of the ridge. In the proximity of the eastern boundary, a secondary maxima appears as a consequence of the upper cloud formation, but only for Experiments 2 and 4.

The amount of rainfall given by the model is sensitive to the surface vegetative cover. The amount of precipitation reaching the surface of the western slope is enhanced when the soil is covered by shrub, while the case with the conifer forest covering the crest of the ridge produces the most rainfall over both slopes.

3.2.4 Surface parameters

Figures 3.11 - 3.13 show the temporal evolution of surface parameters at three locations on the montain barrier: one at the top of the ridge (Top), and two others at an elevation of 200 m (East and West). It should be noted that atmospheric and sub-surface soil models are fully coupled and interactive. Near ground gradients of temperature and moisture depend not only on the evolving structure of the atmospheric wave, but also on other factors such as rain which is absorbed by the soil and accumulated on the leaves of the surface vegetation.

Figure 3.11 shows the diurnal curves of net radiation at the surface for the saturated cases. The curves for the dry case (not shown), revealed that there is net loss during the beginning and ending stages of the simulation in which the sun angle is still low, but high positive values occur during the central part of the day (up to 550 Wm^{-2} at noon) when the solar radiation reaches the ground without significant atmospheric absorption.

However, as can be seen in Fig. 3.11, significant radiative loss does not occur in the saturated cases owing to the downward long wave reemission by atmospheric water vapor. On the other hand, the atmospheric water constituents (vapor and liquid water)

exert an important attenuation of the solar radiation, and the net radiation at the surface is therefore reduced.

The liquid water of clouds is a major factor in determining the amount of solar radiation reaching the ground. The diurnal curves for the three experiments at sites covered by dense clouds (West and Top) are nearly identical, although higher values are obtained over the Top where there is less cloud water in the column of air above the summit. However, over the Eastern slope the net radiative energy for case 3 differs appreciably from the values obtained for cases 2 and 4. As noted in the previous section, the cloud generated by the mountain wave downwind of the barrier is not as well developed in case 3 and the net radiation at the surface exceeds that obtained for cases 2 and 4 by 100 Wm^{-2} at noon.

The uniformity in net radiation previously noted also applies to the ground temperatures for the Top and West locations, except that the case with bare soil yields slightly higher temperatures (Fig. 3.12). The effect of vegetation is to reduce the thermal oscillation during midday, since part of the incoming radiation is consumed by vegetative processes. For all cases, the daytime temperature increase for those locations is less than 1.5 K. For the East location where the solar radiation arrives less attenuated, the daytime increase exceeds 2 K, but the curves are more complex owing to the absorption of the enhanced incoming solar radiation by the vegetative surface.

Figure 3.13 shows that at the height of 15 m, corresponding to the first computational level of the atmospheric model, the temperature is nearly identical for the three simulations. The maximum temperatures are reached at 1300 LST, but there is a significant difference between the values on the eastern and western slopes, with the air over the eastern slope being warmer by 3 K. This fact reflects the wave-induced heating associated with the foehn effect.

Another important aspect is the energy partition between the transpiration (latent heat flux) and the sensible heat fluxes in areas covered by vegetation. This partition is controlled primarily by the leaf stomatal resistance (Pinty et al. 1989). Figures 3.14 and 3.15 show the temporal variation of both fluxes for a conifer forest and for the case of shrub covering the top of the ridge. The result is consistent with their different minimum stomatal resistances given in Table 3.3. Since the stomatal resistance is larger for shrubs than for conifer trees, the transpiration for the shrub covered surface is lesser, resulting in a smaller latent heat flux. On the other hand, the sensible heat flux is greater for shrubs than for conifer trees.

3.2.5 Drag and model adjustment

A measure of the strength of the wave response is the surface pressure drag across the ridge. This is defined by

$$D = \int_0^L \pi \frac{\partial z_s}{\partial x}\, dx$$

where L is the length of the domain. The time-dependent development of the pressure drag for the different experiments is shown in Fig. 3.16. After a period of adjustment, the four simulated mountain waves reach a nearly stationary state before the end of the simulations. The drag value that is ultimately reached in the dry case ($0.16\ 10^6 kg\ s^{-2}$) is

practically the same as in the moist cases, even though the tendencies prior to 1200 LST are different. A possible explanation for that result could be the foehn effect previously mentioned. Although the difference of pressures between both sides of the ridge induced by the wave itself is larger for a dry atmosphere, there is at the same time in the moist cases another mechanism which tends to accentuate that difference by lowering the pressure above the lee slope. That air is warmer and less dense and therefore serves to compensate for the stronger dynamic effect of the dry wave.

An important consideration in the assessment of the results is the time required for the model to adjust to the initial conditions. The fact that the wave intensity decreases for the four cases simulated between the times considered (1200 and 1800 LST), could be taken as a consequence of the model adjustment. However, the adjustment of the surface drag to near equilibrium values in only one hour suggests that the spin-up process does not significantly affect the results. That initial assessment was subsequently confirmed by carrying out Experiment 3 for a period of 48 hours. The fields for the second day of simulation (not shown) are nearly indistinguishable from those presented above, indicating that the temporal evolution of the fields represents the effects of temporal changes in the boundary layer rather than a model adjustment process. That conclusion is confirmed in Fig. 3.17 which presents the surface drag for that period of 48 hours. The uniformity of the drag after 1800 LST indicates that the model has completely adjusted. The appearance of a slight dome in the curve on the second day is attributed to a new strengthening of the wave.

3.3 Conclusions

A two-dimensional meso-β model with a coupled soil and vegetation sub-model has been used to study the effects of different vegetative surfaces on orographically generated atmospheric waves. In the absence of vegetation but with a moist soil, the atmospheric wave structure for both dry and saturated atmosphere is in good agreement with previous studies (Nickerson et al. 1986), but shows a redistribution of winds at low levels owing to a more realistic treatment of the ground temperature which is allowed to vary in response to the evolving surface energy fluxes.

The inclusion of dense vegetation in the simulation of mountain waves reveals a great sensitivity of the airflow and thermal structure at all levels of the model to the treatment of the lower boundary. A tall, dense vegetative surface such as a conifer forest significantly diminishes the intensity of the mountain wave. As a result of a higher symmetry of isotachs between both slopes at low levels, this case corresponds to a diminution of the stronger downslope surface winds, and the creation of an extensive layer of vertical wind shear in the proximity of the summit. That deep layer of strong wind shear in the low atmosphere, combined with low stability, seems to be an important agent in the development of turbulence. The reduction in atmospheric stability associated with foehn conditions in a moist environment has important consequences for the development of turbulence downwind of a mountain barrier.

The model-predicted rainfall suggests an important role for vegetation in the development of clouds and the enhancement of precipitation. When the surface is covered by

shrub, enhanced rainfall occurs from the orographic cloud that develops over the upwind slope. But when the shrub on the crest of the mountain is replaced by a conifer forest as typically occurs in many parts of the world, the rainfall over the upwind and downwind slopes is enhanced.

The results obtained in this work show the importance of surface induced frictional effects on the simulation of surface airflow, stability and turbulent kinetic energy of orographically forced circulations. Improved simulations and model predictions of airflow over mountainous terrain will require an adequate treatment of the vegetative canopy in the surface energy budget calculation. In particular, a realistic specification of the roughness length, explicitaly when simple parameterizations for the surface layer are used, or implicitaly through an adequate knowledge of the vegetation cover in the area of interest if complet parameterizations are included, seems necessary. These findings may be particularly relevant to studies of atmospheric dispersion in the PBL over complex vegetative surfaces.

ν	σ
0.0000	0.0000
0.0333	0.0444
0.1000	0.1333
0.1667	0.2220
0.2333	0.3101
0.3000	0.3973
0.3667	0.4829
0.4333	0.5660
0.5000	0.6458
0.5667	0.7212
0.6333	0.7908
0.7000	0.8533
0.7667	0.9071
0.8333	0.9504
0.9000	0.9813
0.9667	0.9978
1.0000	1.0000

Table 3.1. Comparison of the ν and σ vertical grids.

Parameter	**Unit**	**Value**
Porosity	—	0.458
Saturated hydraulic conductivity	$.10^{-6}$ m s^{-1}	5.65
Saturated moisture potential	m	-0.548
Dry volumetric heat capacity	$.10^{6}$ J m^{-3} K^{-1}	1.242
Exponent b	—	6.58
Emissivity	—	0.99
Albedo	—	0.14
Roughness length	m	0.005

Table 3.2. Mixed soil characteristics.

Parameter	Unit	CONIFER FOREST	SHRUB
Height	m	20.0	0.5
Displacement height	m	15.0	0.37
Plant resistance	s	8.10^9	10.10^9
Minimum stomatal resistance	s m^{-1}	350	500
Critical leaf water potential	m	-150	-150
Green leaf area index	—	3.5	1.0
Dry leaf area index	—	0.7	2.0
Rooting depth	m	0.8	0.4
Emissivity	—	0.98	0.98
Albedo	—	0.10	0.16
Roughness length	m	1.67	0.04

Table 3.3. Specification of vegetative characteristics in Experiments 3 and 4.

Experiment	Atmosphere	Zone	Vegetation type	Shielding factor
1	Dry	Top	—	—
		Slopes	—	—
2	Saturated	Top	—	—
		Slopes	—	—
3	Saturated	Top	Conifer Forest	0.9
		Slopes	Shrub	0.8
4	Saturated	Top	Shrub	0.8
		Slopes	Shrub	0.8

Table 3.4. Summary of the numerical experiments.

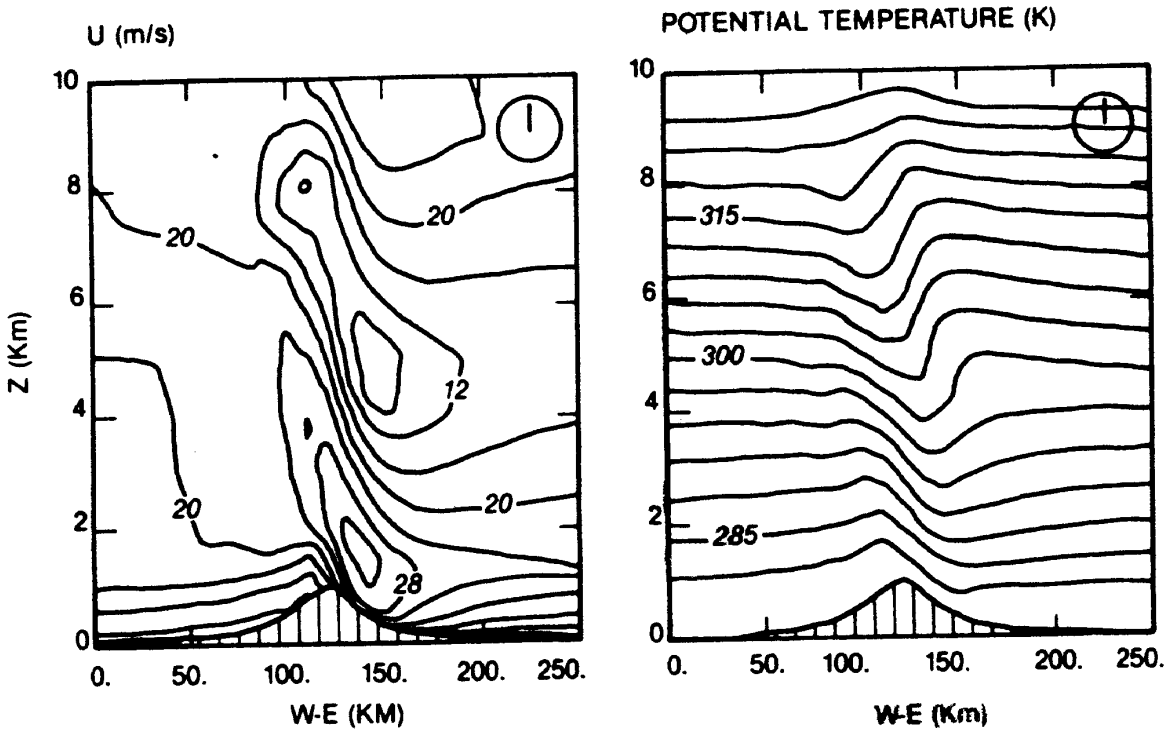

FIG. 3.1a. Horizontal velocity and potential temperature for the dry case (Nickerson et al. 1986).

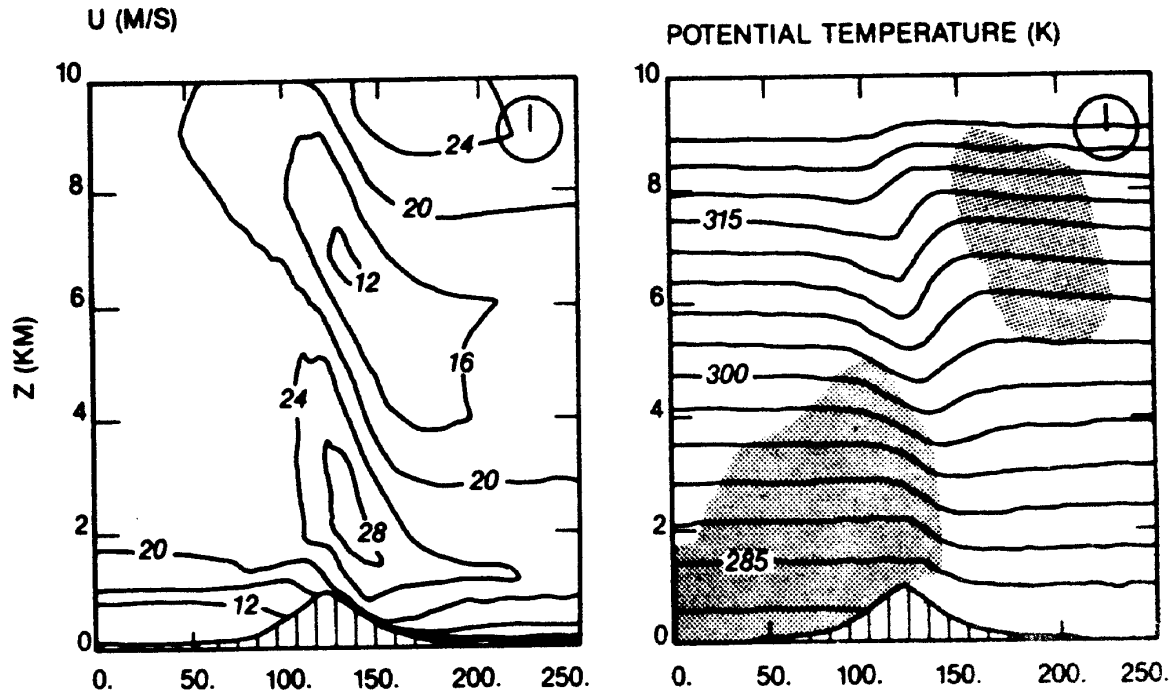

FIG. 3.1b. As in Fig. 3.1a, but for the moist case (Nickerson et al. 1986).

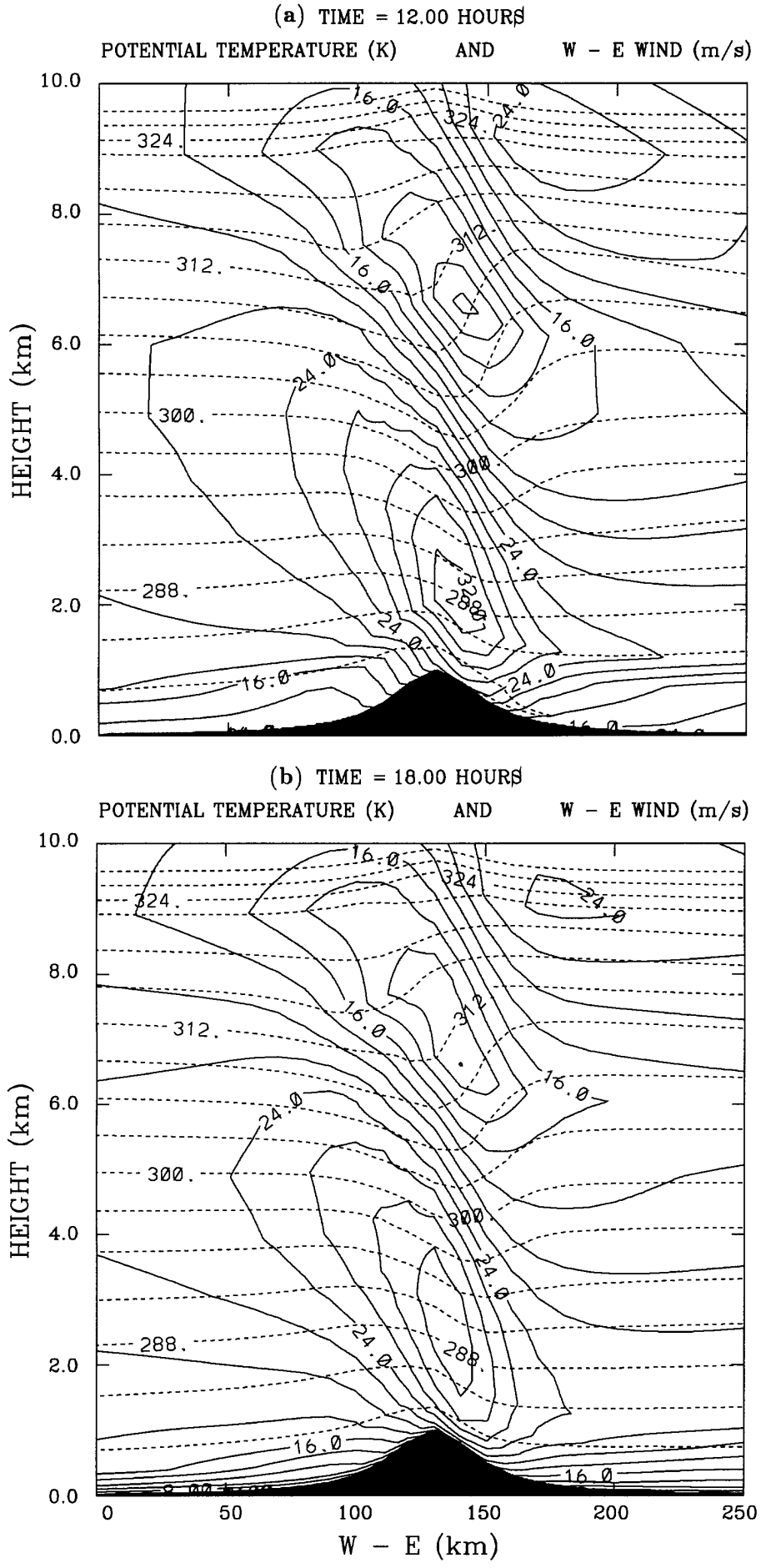

FIG. 3.2. Vertical cross section showing W-E horizontal velocity (solid line) and potential temperature (dashed line) for **Experiment 1**: (**a**) at 1200 LST, (**b**) at 1800 LST.

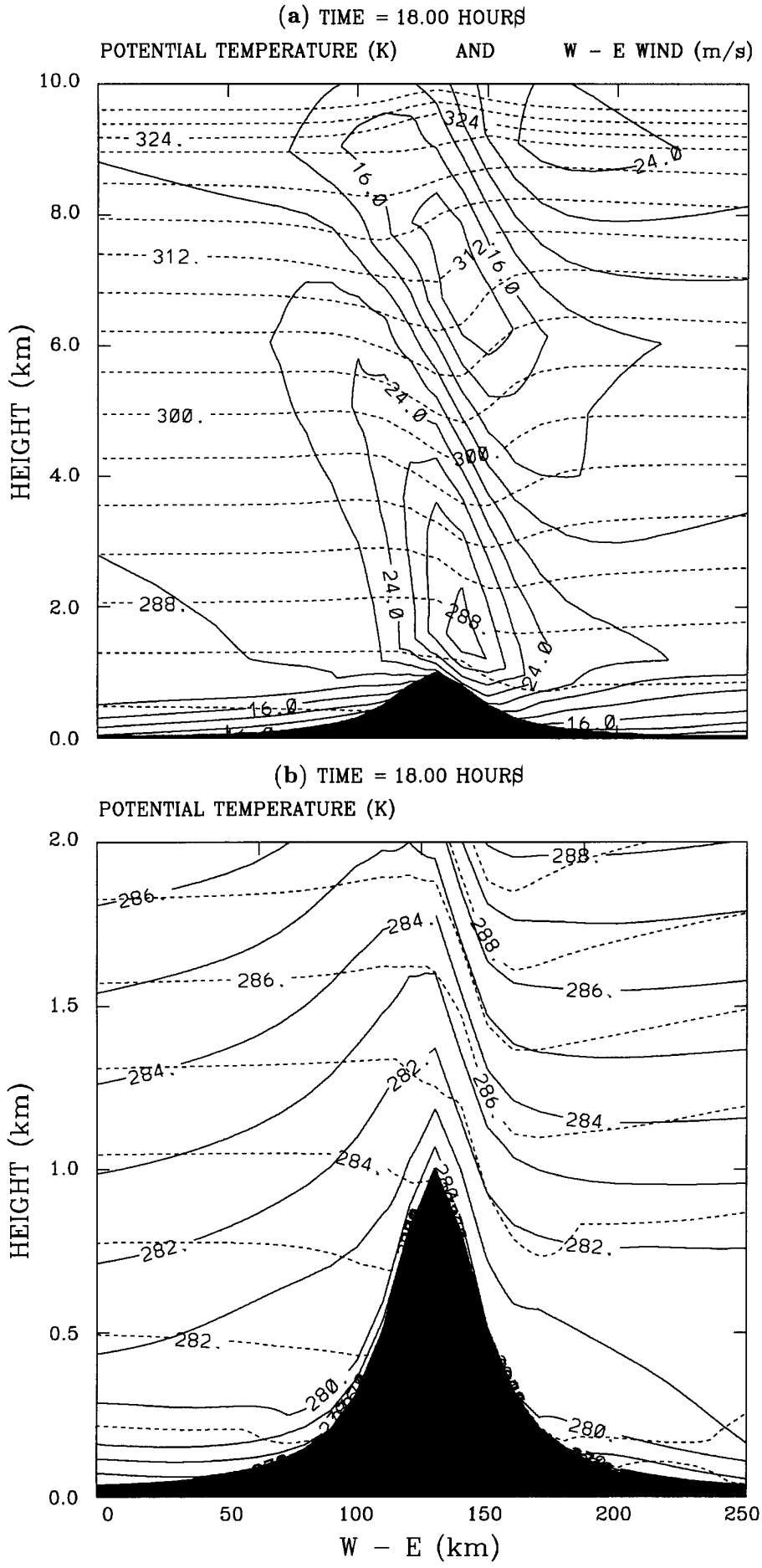

FIG. 3.3. (a) As in Fig. 3.2 but for **Experiment 2** at 1800 LST. (b) Detailed view of potential temperature around the mountain for Experiments 1 (solid line) and 2 (dashed line) at 1800 LST.

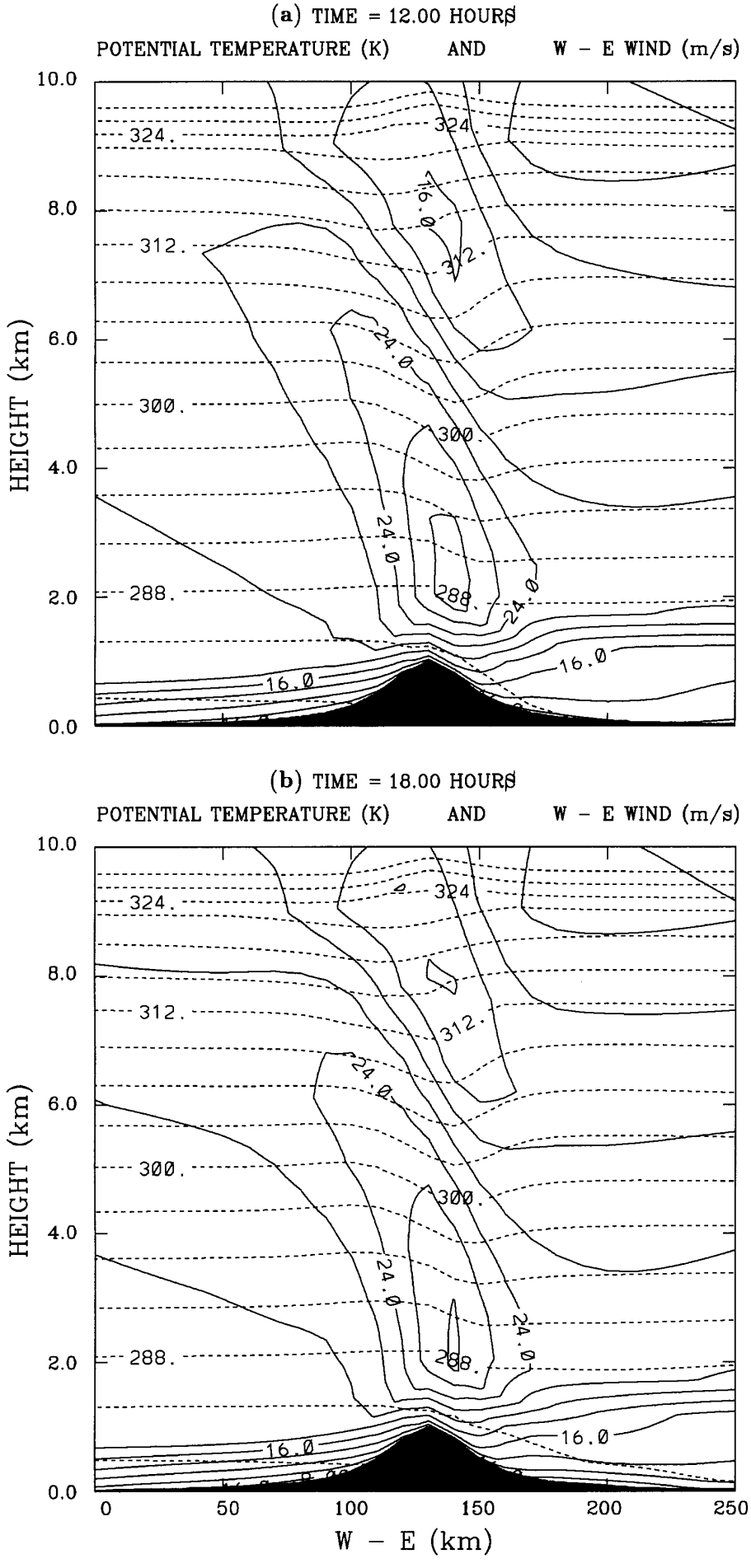

FIG. 3.4. As in Fig. 3.2 but for **Experiment 3**: (**a**) at 1200 LST, (**b**) at 1800 LST.

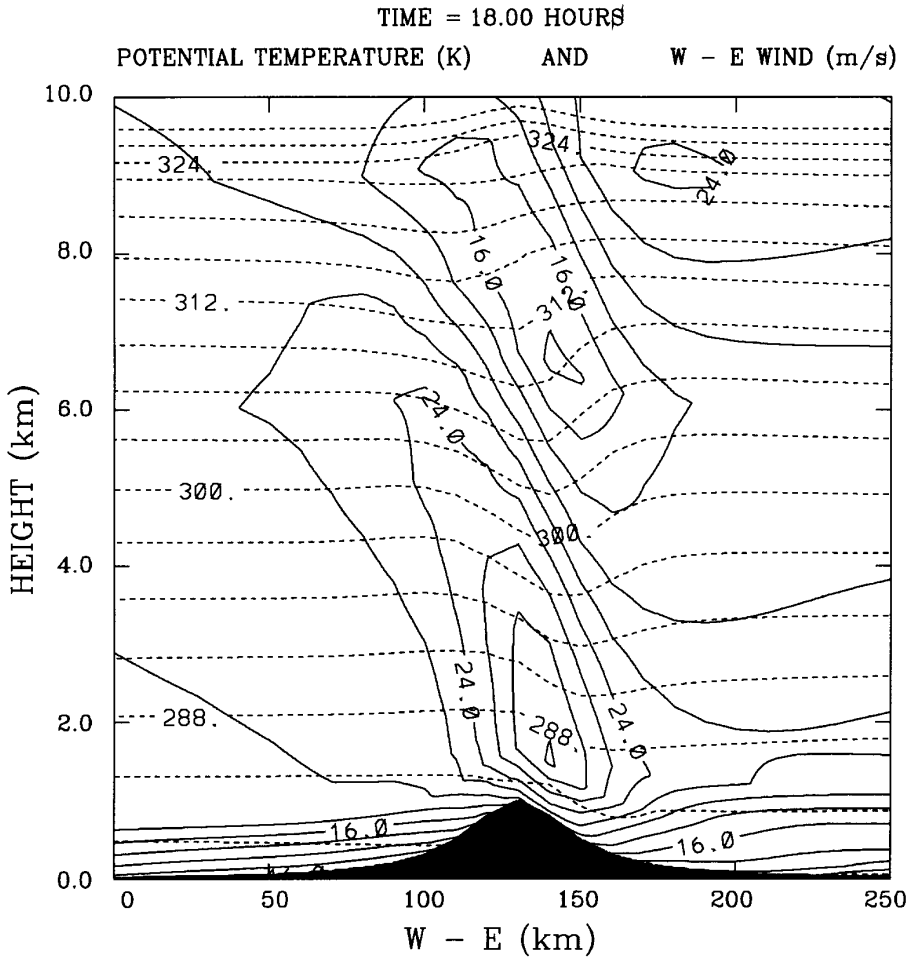

FIG. 3.5. As in Fig. 3.2 but for **Experiment 4** at 1800 LST.

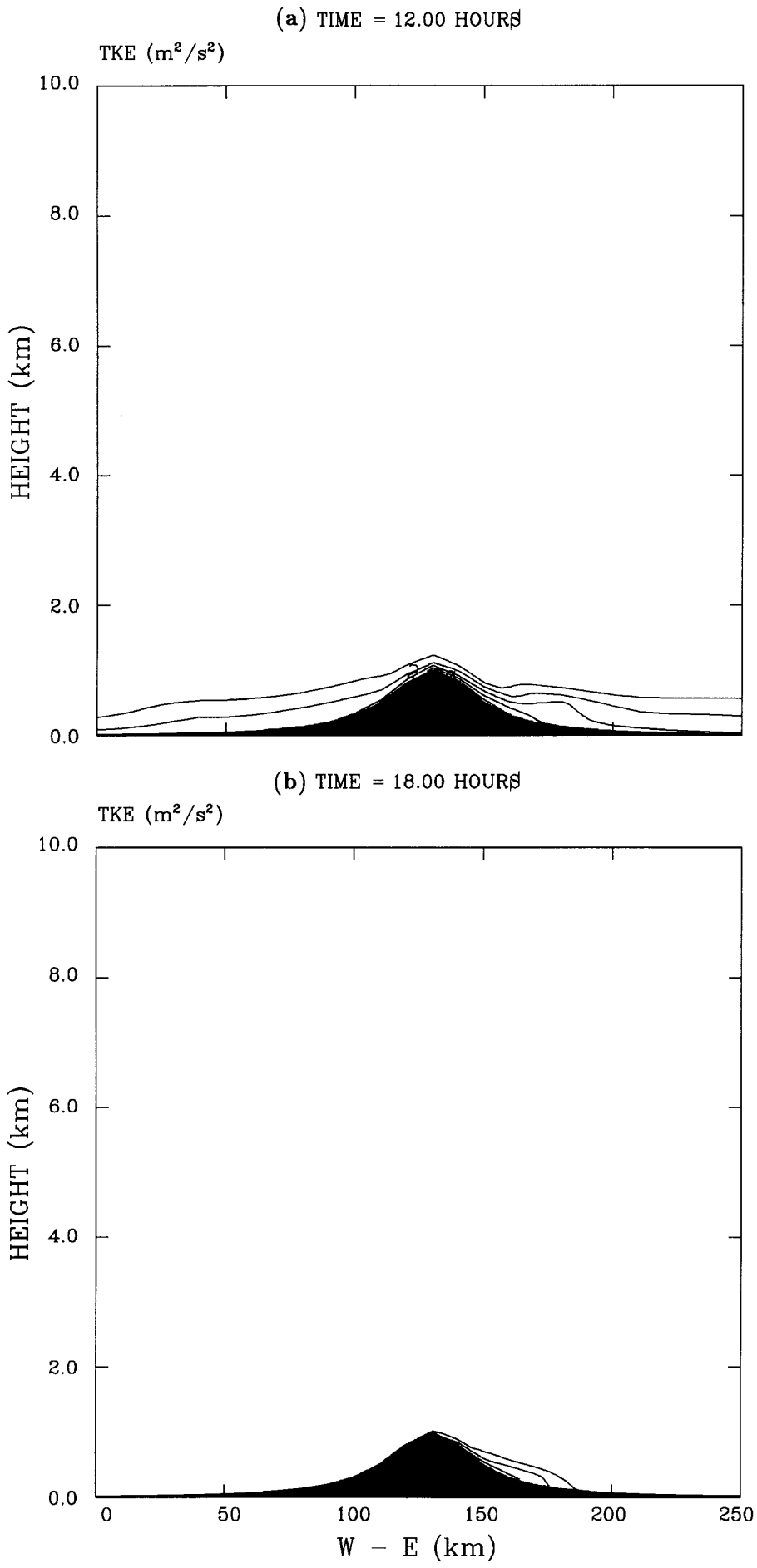

FIG. 3.6. Vertical cross section of the turbulent kinetic energy field for **Experiment 1**: (**a**) at 1200 LST, (**b**) at 1800 LST. The contours are drawn every 0.5 $m^2 s^{-2}$ starting at 0.5 $m^2 s^{-2}$.

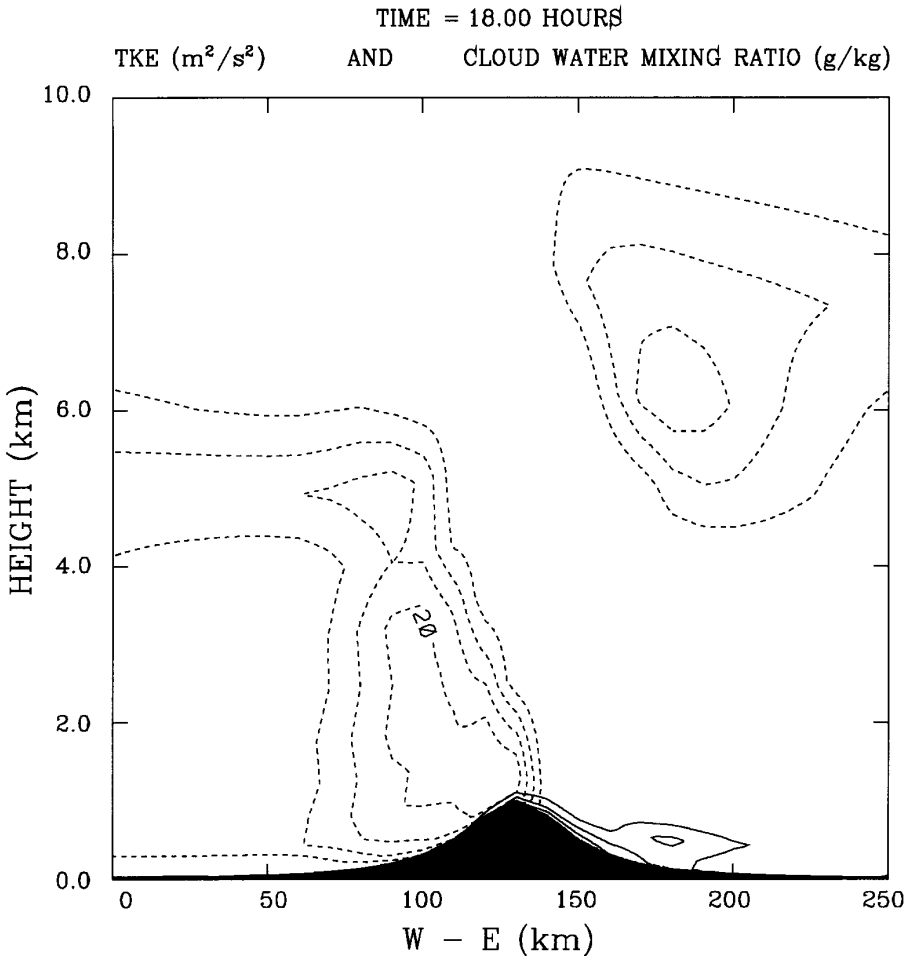

FIG. 3.7. Vertical cross section of the turbulent kinetic energy field (solid line) and cloud water mixing ratio (dashed line) for **Experiment 2** at 1800 LST. The solid contours are drawn every 0.5 m^2s^{-2} starting at 0.5 m^2s^{-2}. The dashed contours are drawn every 0.05 gkg^{-1} starting at 0.05 gkg^{-1}.

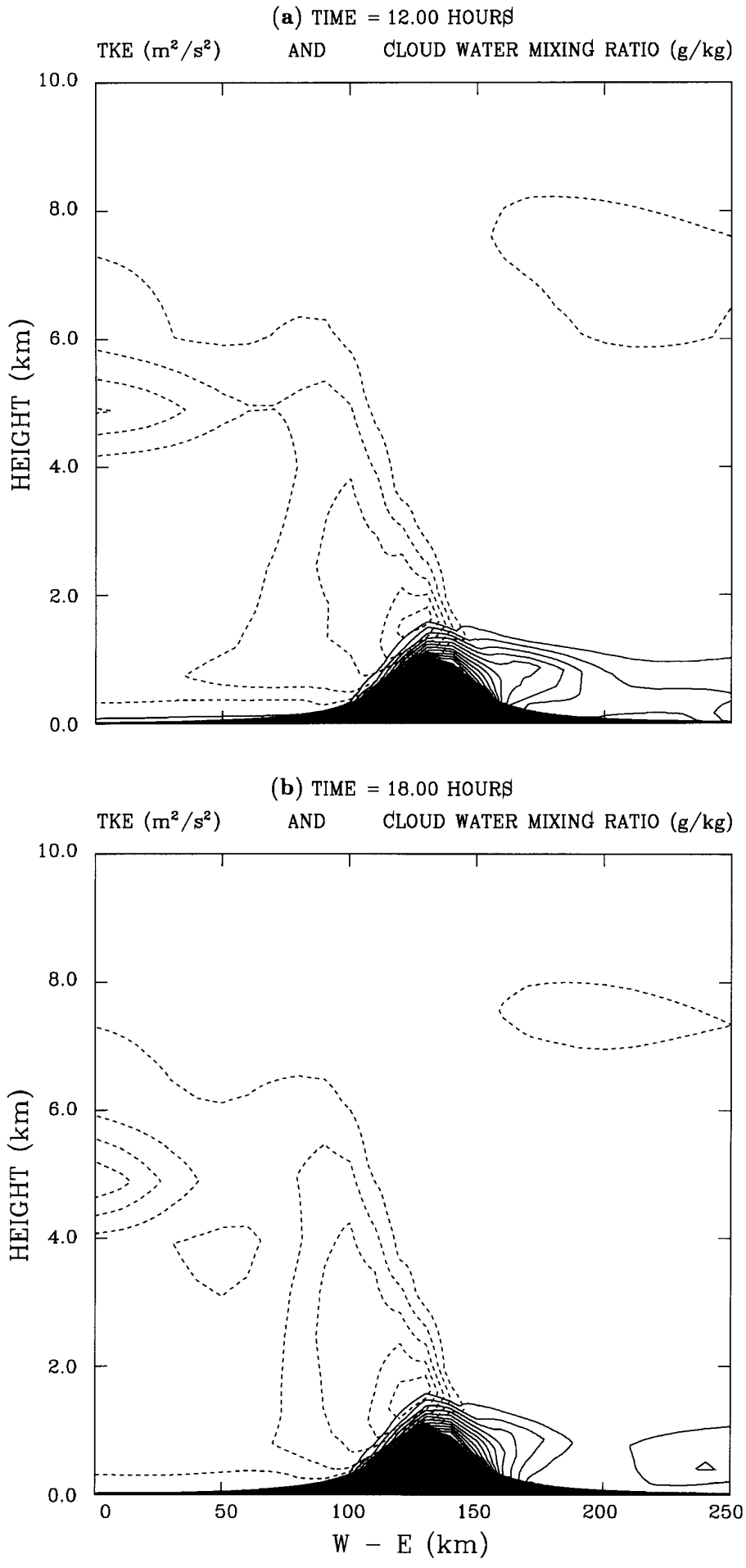

FIG. 3.8. As in Fig. 3.7 but for **Experiment 3**: (**a**) at 1200 LST, (**b**) at 1800 LST.

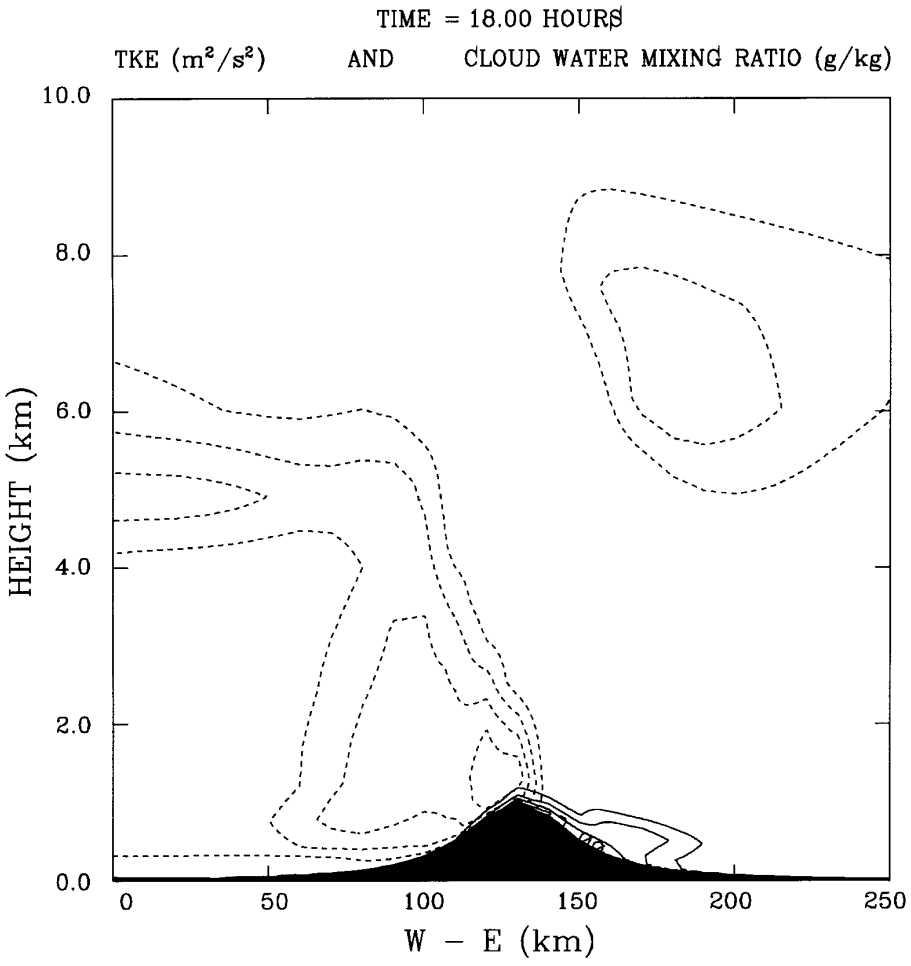

FIG. 3.9. As in Fig. 3.7 but for **Experiment 4** at 1800 LST.

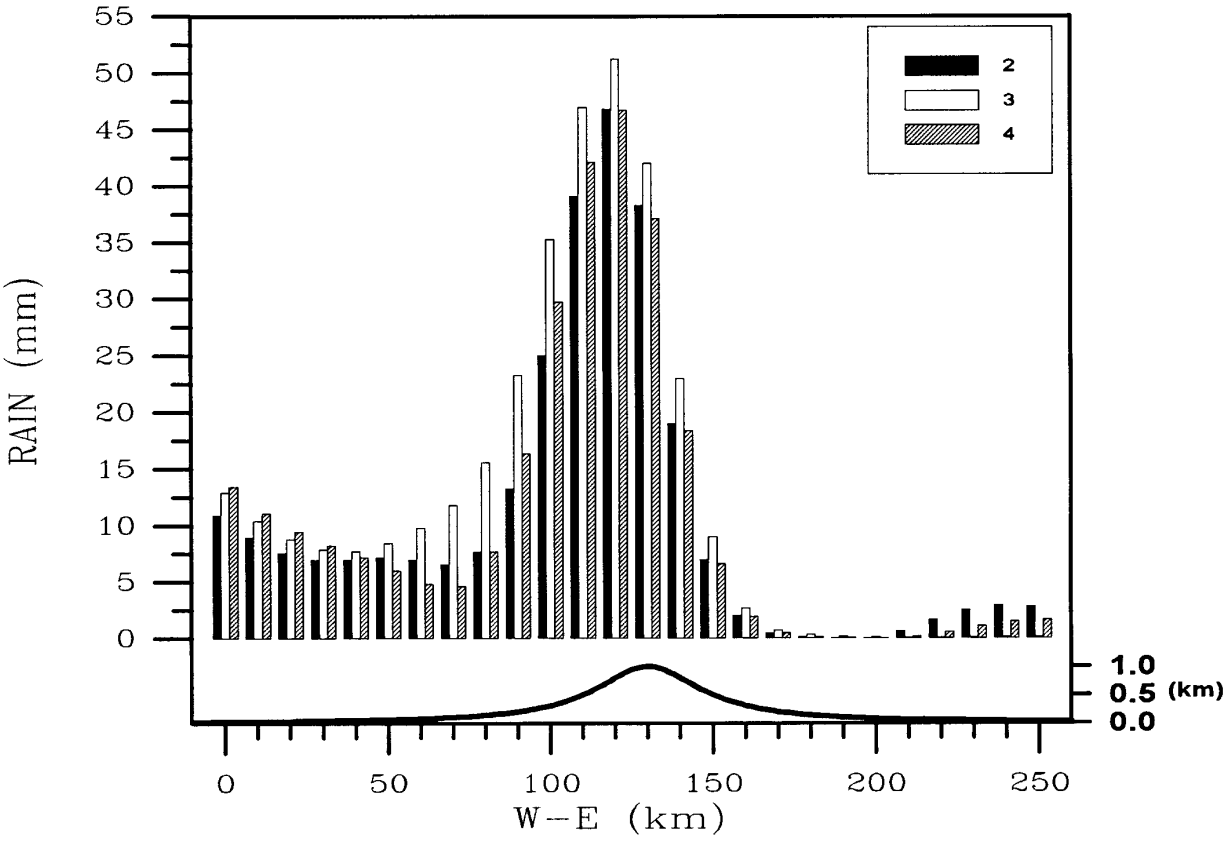

FIG. 3.10. Model predicted rainfall after the period of simulation for Experiments 2, 3 and 4 (black, white and gray bars respectively).

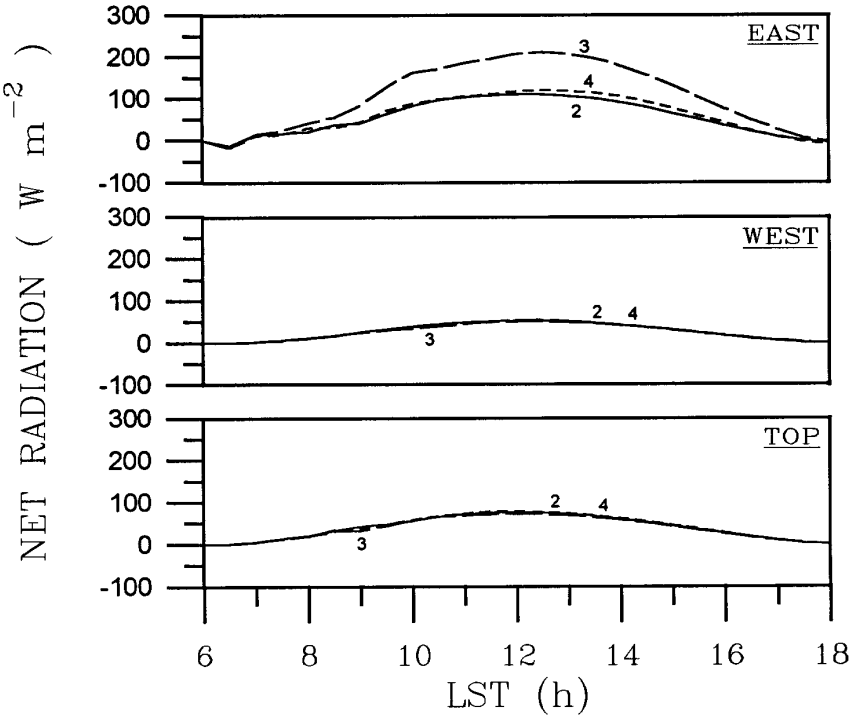

FIG. 3.11. Time evolution of the net radiation at the surface for Experiments 2 (solid line), 3 (long dashes) and 4 (short dashes): in the top of the ridge (TOP), at an elevation of 200 m on the west slope (WEST), in the symmetric point on the east slope (EAST).

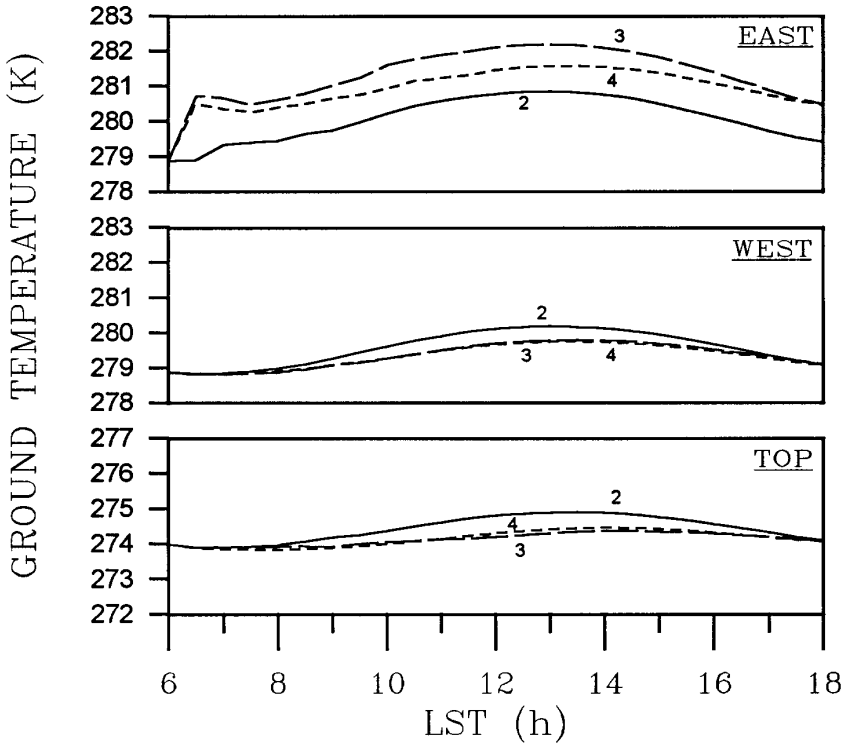

FIG. 3.12. As in Fig. 3.11 except for the ground temperature.

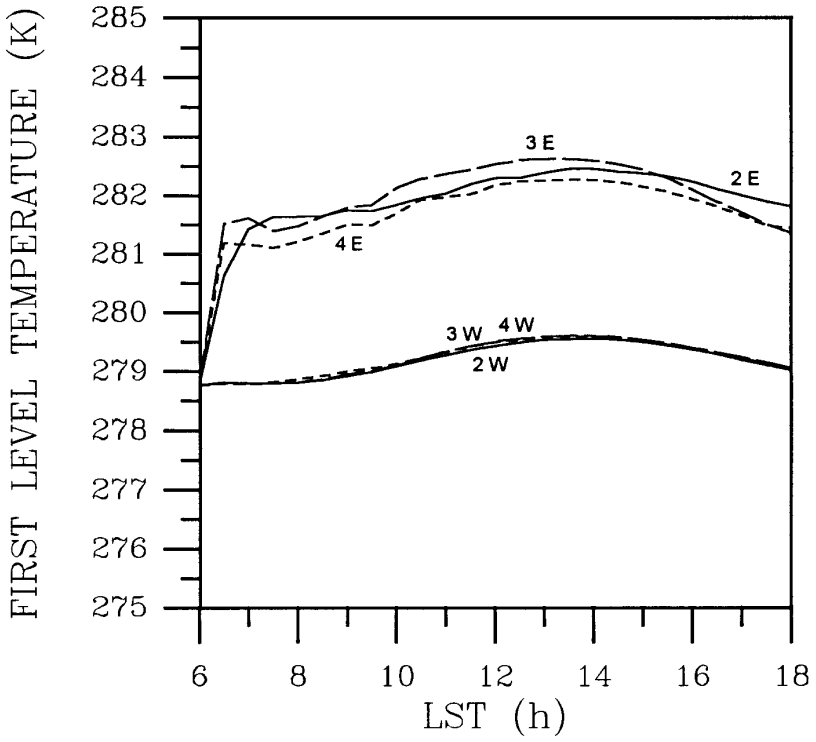

FIG. 3.13. Time evolution of the air temperature given by the model at the first computational level (15 m above the ground approximately) over both slopes, for Experiments 2 (solid line), 3 (long dashes) and 4 (short dashes). E and W refer to the east and west slope respectively.

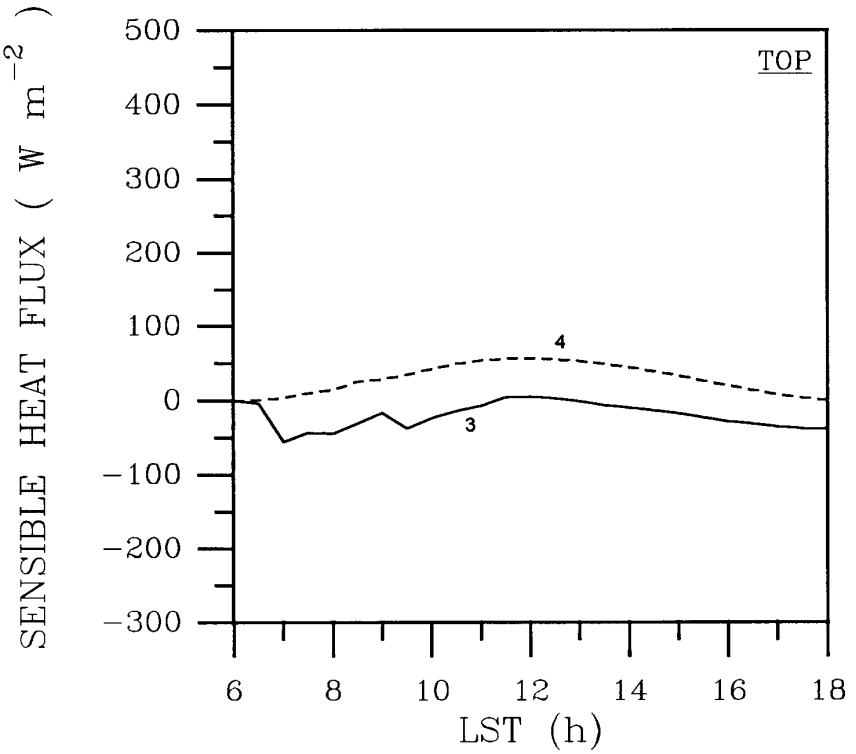

FIG. 3.14. Time evolution of the surface sensible heat flux for Experiments 3 (solid line) and 4 (dashed line) at the top of the ridge.

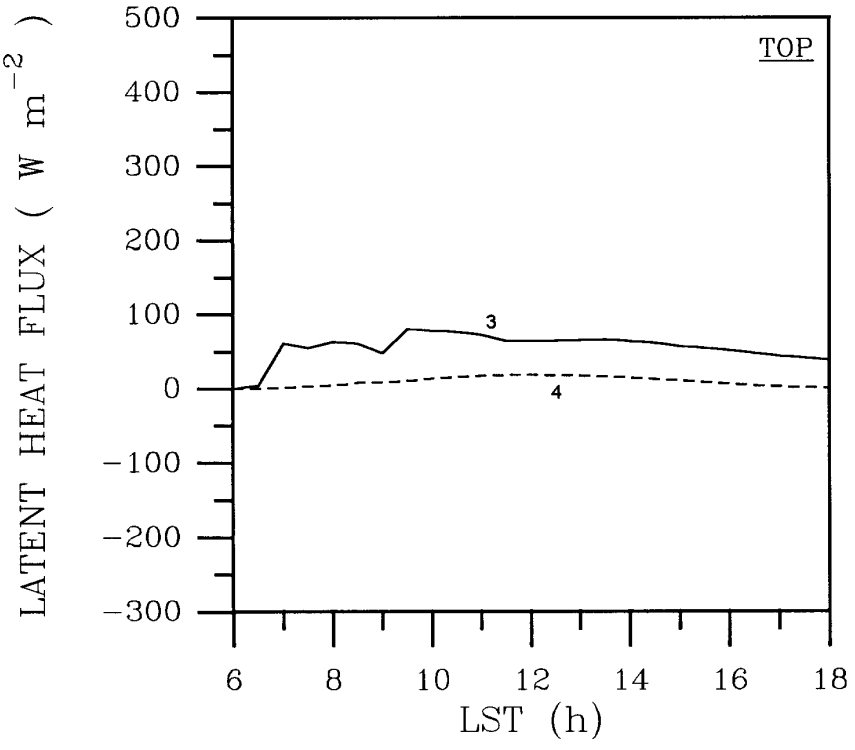

FIG. 3.15. As in Fig. 3.14 except for the latent heat flux.

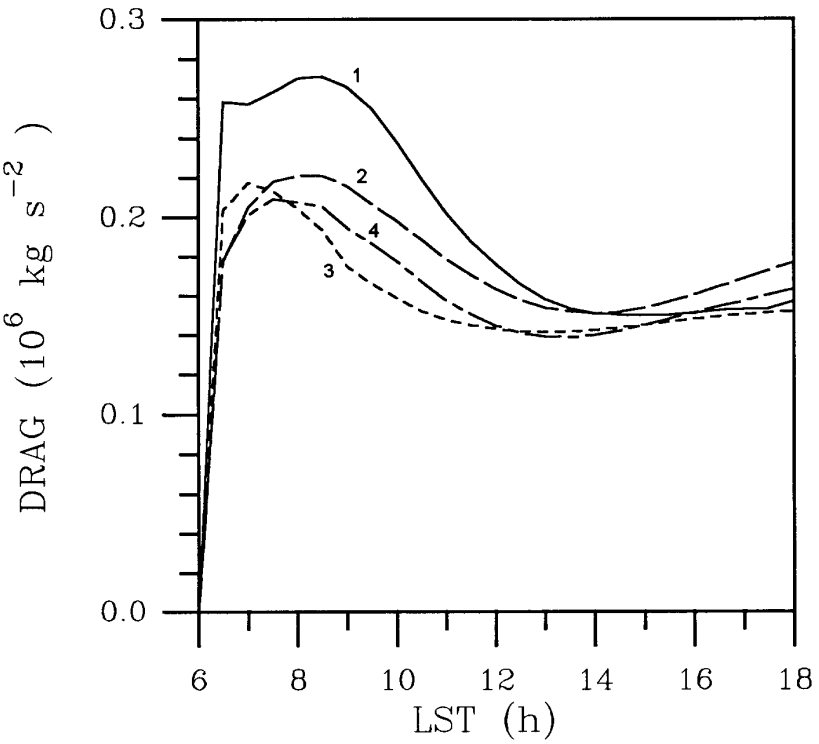

FIG. 3.16. Time evolution of the surface pressure drag across the ridge for Experiments 1 (solid line), 2 (long dashes), 3 (short dashes) and 4 (long and short dashes).

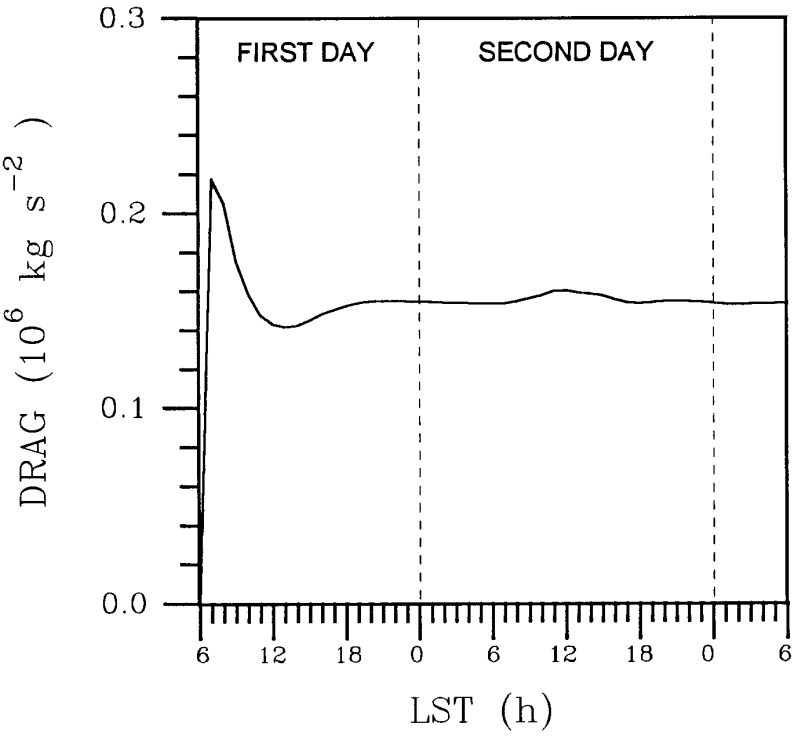

FIG. 3.17. Time evolution of the surface pressure drag for a simulation of 48 hours for Experiment 3.

APPENDIX 1

List of Symbols

a	half width of the ridge
B	vertical scale factor
C_p	specific heat at constant pressure
C_ϵ	numerical coefficinet for the TKE dissipation term
$D_{\pi u}$, $D_{\pi v}$, D_S, D_W, $D_{\pi q_r}$, $D_{\pi N_r}$, $D_{\pi e}$	horizontal difussion terms
e	turbulent kinetic energy
e_s	saturation vapor pressure
$F_{\pi u}$, $F_{\pi v}$, F_S, F_W, $F_{\pi q_r}$, $F_{\pi N_r}$, $F_{\pi e}$	turbulent mixing terms
f	Coriolis parameter
g	acceleration of gravity
h	maximum height of the ridge
H	entropy
K_m, K_θ, K_e	exchange coefficients
l_k	mixing length scale
l_ϵ	dissipation length scale
L_v	latent heat
N_r	number of raindrops concentration
P	pressure
P_0	reference pressure = 1000 hPa
P_s	surface pressure
P_t	pressure at the upper boundary = 100 hPa
$\hat{P}$	$\left(\frac{P}{P_0}\right)^{R_v/C_p}$
q_{cw}	cloud water mixing ratio
q_r	rainwater mixing ratio
q_v	water vapor mixing ratio
q_{vs}	saturation water vapor mixing ratio
R_L	incoming longwave radiation at the surface
R_S	incoming solar radiation at the surface
R_v	universal gas constant
S	entropy variable defined by $S = \pi H$
S_S, S_W, $S_{\pi q_r}$, $S_{\pi N_r}$	source-sink terms
t	time
T	temperature
T_0	reference temperature = 273.16 K
T_s	saturation temperature
T^*	virtual temperature
u	wind component along the x-coordinate
v	wind component along the y-coordinate

W	moisture variable defined by $W = \pi(q_v + q_{cw})$
x	coordinate in the west-east direction
y	coordinate in the south-north direction
z_s	surface height
Δt	time step
Δx	horizontal grid length
γ_{cg}	temperature countergradient
π	$(P_s - P_t)$
σ	pressure coordinate defined by $\sigma = (P - P_t)/\pi$
σ'	$d\sigma/d\nu$
ν	vertical coordinate related with σ by $\sigma = (4\nu - \nu^4)/3$
$\dot{\nu}$	vertical velocity
ϕ	geopotential
ρ	density of air
ρ_l	density of liquid water
θ	potencial temperature
θ_v	virtual potential temperature. $\theta_v = \theta(1 + 0.61q_v)$

REFERENCES

Anthes, R. A., and T. T. Warner, 1974: *Prediction of mesoscale flows over complex terrain.* ECOM Technical Report No. 5532, White Sands Missile Range, New Mexico 88002.

Anthes, R. A., and T. T. Warner, 1978: Development of hydrodynamic models suitable for air pollution and other mesometeorological studies. *Mon. Wea. Rev.*, **106** 1045-1078.

Atkinson, B. W., 1981: *Mesoscale atmospheric circulations.* Academic Press, New York, 495 pp.

Bacmeister J., 1987: *Nonlinearity in transient, two dimensional flow over topography.* PhD thesis, Princenton University.

Baines, P. G., and T. N. Palmer, 1990: *Rationalle for a new physically-based parameterization of subgridscale orographic effects.* ECMWF Tech. Mem. No. 169.

Banta, R. M., 1990: The role of mountain flows in making clouds (Chapter 9 in *Atmospheric processes over complex terrain*), American Meteorological Society, volume 23, number 45. Willian Blumen Editor.

Beard, K. V., and H. R. Pruppacher, 1969: A determination of the terminal velocity and drag of small water drops by means of a wind tunnel. *J. Atmos. Sci.*, **26,** 1066-1072.

Berry, E. X., 1967: Cloud droplet growth by collection. *J. Atmos. Sci.*, **24,** 688-701.

Berry, E. X., and R. L. Reinhardt, 1973: *Modeling of condensation and collection within clouds.* D.R.I. Phys. Sci. Pub. No.16, University of Nevada.

Berry, E. X., and M. P. Pranger, 1974: Equations for calculating the terminal velocities of water drops. *J. Appl. Meteor.*, **13,** 108-113.

Bougeault, P., and P. Lacarrère, 1989: Parameterization of orographic induced turbulence in a mesobeta scale model. *Mon. Wea. Rev.*, **117,** 1872-1890.

Bougeault, P., A. Jansà, B. Benech, B. Carissimo, J. Pelon and E. Richard, 1990: Momentum budget over the Pyrenees: the PYREX experiment. *Bull. Amer. Meteor. Soc.*, **71,** 806-818.

Businger, J. A., J. C. Wyngaard, Y. Izumi and E. F. Bradley, 1971: Flux-profile relationship in the atmospheric surface layer. *J. Atmos. Sci.*, **28,** 181-189.

Davies, H. C., 1976: A lateral boundary formulation for multi-level prediction models. *Quart. J. R. Meteor. Soc.*, **102,** 405-418.

Deardorff, J. W., 1972: Theoretical expressions for the counter gradient vertical heat flux. *J. Geophys. Res.*, **30,** 5900-5904.

Deardorff, J. W., 1978: Efficient prediction of ground surface temperature and moisture, with inclusion of a layer of vegetation. *J. Geophys. Res.*, **83,** 1889-1903.

De Rivas, E. K., 1972: On the use of nonuniform grids in finite difference equations. *J. Comput. Phys.*, **10,** 202-210.

Dufour, L., and J. Van Mieghem, 1975: *Thermodynamique de l'atmosphere*. Institut Royal Meteoroologique de Belgique, Brussels.

Durran, D. R., and J. B. Klemp, 1983: A compressible model for the simulation of moist mountain waves. *Mon. Wea. Rev.*, **111,** 2341-2361.

Durran, D. R., 1986: Mountain Waves. *Mesoscale Meteorology and Forecasting*, P. Ray, Ed., Amer. Meteor. Soc., 472-492.

Durran, D. R., 1990: Mountain waves and downslope winds (Chapter 4 in *Atmospheric processes over complex terrain*), American Meteorological Society, volume 23, number 45. Willian Blumen Editor.

Gill, A., 1982: *Atmosphere-Ocean Dynamics*, Academic Press, 662 pp.

Gunn, R., and G. D. Kinzer, 1949: The terminal velocity of fall for water droplets in stagnant air. *J. Meteor.*, **6,** 243-248.

Hanna, S. R., and D. G. Strimaitis, 1990: Rugged terrain effects on diffusion. Atmospheric processes over complex terrain (Chapter 6), *American Meteorological Society*, volume 23, number 45. Willian Blumen Editor.

Klemp, J. B., and D. K. Lilly, 1978: Numerical simulation of hydrostatic mountain waves. *J. Atmos. Sci.*, **35,** 78-107.

Laprise, R., and W. R. Peltier, 1989: On the structural characteristics of steady finite-amplitude mountain waves over bell-shaped topography. *J. Atmos. Sci.*, **46,** 586-595.

Lilly, D. K., and E. J. Zipser, 1972: The front range windstorm of 11 January 1972. A meteorological narrative. *Weatherwise*, **25,** 56-63.

Lilly, D. K., 1978: Analysis of an intense mountain wave and aircraft turbulence. *J. Atmos. Sci.*, **35,** 59-77.

Long, R. R., 1953: Some aspects of the flow of stratified fluids. A theoretical investigation. *Tellus*, **5,** 42-58.

Louis, J. F., 1979: A parametric model of vertical eddy fluxes in the atmosphere. *Bound. Layer Meteor.*, **17,** 187-202.

Mahfouf, J. F., E. Richard and P. Mascart, 1987a: The influence of soil and vegetation on the development of mesoscale circulations. *J. Climate Appl. Meteor.*, **26,** 1483-1495.

Mahfouf, J. F., E. Richard, P. Mascart, E. C. Nickerson and R. Rosset, 1987b: A comparative study of various parameterizations of the planetary boundary layer in a numerical mesoscale model. *J. Climate Appl. Meteor.*, **26,** 1671-1695.

Mahrer, Y., and R. A. Pielke, 1977: The effects of topography on the sea and land breezes in a two-dimensional numerical model. *Mon. Wea. Rev.*, **105,** 1151-1162.

Mahrer, Y., and R. A. Pielke, 1978: A test of an upstream spline interpolation technique for the advective terms in a numerical mesoscale model. *Mon. Wea. Rev.*, **106,** 818-830.

Markowitz, A. H., 1976: Raindrop size distribution expressions. *J. Appl. Meteor.*, **15,** 1029-1031.

McCumber, M. C., and R. A. Pielke, 1981: Simulation of the effects of surface fluxes of heat and moisture in a mesoscale numerical model: 1. Soil Layer. *J. Geophys. Res.*, **86,** 9929-9938.

McFarlane, N. A, 1987: The effect of orographically excited gravity wave drag on the general circulation of the lower stratosphere and troposphere. *J. Atmos. Sci.*, **44,** 1775-1800.

Miles, J. W., and H. E. Huppert, 1969: Lee waves in a stratified flow. Part 4: Perturbation aproximations. *J. Fluid Mech.*, **35,** 497-525.

Murray, F. W., 1967: On the computation of saturation vapor pressure. *J. Appl. Meteor.*, **6,** 203-204.

Nickerson, E. C., and E. L. Magaziner, 1976: *A three-dimensional simulation of winds and non-precipitating orographic clouds over Hawaii.* NOAA Technical Report ERL 377-APCL 39, 35 pp.

Nickerson, E. C., 1979: On the numerical simulation of airflow and clouds over mountainous terrain. *Beitr. Phys. Atmos.*, **52,** 161-177.

Nickerson, E. C., E. Richard, R. Rosset and D. R. Smith, 1986: The numerical simulation of clouds, rain and airflow over the Vosges and Black Forest mountain: a meso-β model with parameterized microphysics. *Mon. Wea. Rev.*, **114,** 398-414.

Orlanski, I., 1975: A rational subdivision of scales for atmospheric processes. *Bull. Am. Met. Soc.*, **56,** 527-530.

Palmer, T. N., G. J. Schutts and R. Swinbank, 1986: Alleviation of a systematic westerly bias in general circulation and numerical weather prediction models through an orographic gravity wave drag parameterization. *Q. J. R. Meteorol. Soc.*, **112,** 1001-1039.

Pielke, R. A., 1984: *Mesoscale meteorological modeling.* Academic Press, Orlando, 612 pp.

Pinty, J. P., P. Mascart, E. Richard and R. Rosset, 1989: An investigation of mesoscale flows induced by vegetation inhomogeneities using an evapotranspiration model calibrated against HAPEX-MOBILHY data. *J. Appl. Meteor.*, **28,** 976-992.

Queney, P., 1948: The problem of air flow over mountain: A summary of theoretical studies. *Bull. Amer. Meteor. Soc.*, **29,** 16-26.

Queney, P., G. Corby, N. Gerbier, H. Koschmieder and J. Zierep, 1960: *The airflow over mountains.* WMO Tech. Note 34., 135 pp.

Ramis, C., and R. Romero, 1995: A first numerical simulation of the development and structure of the sea breeze in the island of Mallorca. *Ann. Geophy.*, (in press).

Richard, E., J. P. Pinty, and N. Chaumerliac, 1985: *Simulations d'ondes de montagne hydrostatiques bidimensionnelles.* Note I.O.P.G. number 82, 41 pp.

Richard, E., N. Chaumerliac, and J. F. Mahfouf, 1986: Numerical simulation of orographic enhancement of rain with a mesoscale model. *J. Climate Appl. Meteor.*, **26,** 661-669.

Richard, E., P. Mascart and E. C. Nickerson, 1989: The role of surface friction in downslope windstorms. *J. Appl. Meteor.*, **28,** 241-251.

Robinson, G., D., 1967: Some current projects for global meteorological observation and experiment. *Quart. J. R. Meteor. Soc.*, **93,** 409-418.

Romero, R., S. Alonso, E. C. Nickerson, and C. Ramis, 1995: The influence of vegetation on the development and structure of mountainn waves. *J. Appl. Meteor.*, **34,** 2230-2242.

Schlesinger, R. F., L. W. Uccellini and D. R. Johnson, 1983: The effects of the Asselin time filter on numerical solutions to the linearized shallow-water wave equations. *Mon. Wea. Rev.*, **111,** 455-467.

Shafrir, U., and M. Neiburger, 1963: Collision efficiencies of two spheres falling in a

viscous medium. *J. Geophys. Res.*, **68,** 4114-4148.

Smith, R. B., 1977: The steepening of hydrostatic mountain waves. *J. Atmos. Sci.*, **34,** 1634-1654.

Smith, R. B., 1979: The influence of mountains on the atmosphere. *Advances in Geophysics*, B. Saltzman, Ed., Vol. 21, Academic Press, 87-230.

Smith, R. B., 1988: Linear theory of stratified flow past an isolated mountain in isosteric coordinates. *J. Atmos. Sci.*, **45,** 3889-3896.

Smith, R. B., 1989a: Mountain induced stagnation points in hydrostatic flow. *Tellus*, **41A,** 270-274.

Smith, R. B., 1989b: Hydrostatic airflow over mountains. *Advances in Geophysics*, **31,** 1-41.

Therry, G., and P. Lacarrère, 1983: Improving the eddy-kinetic energy model for planetary boundary layer description. *Bound. Layer Meteor.*, **25,** 63-88.

Tripoli, G., J., and W. R. Cotton, 1989: Numerical study of an observed orogenic mesoscale convective system. Part I: Simulated genesis and comparison with observations. *Mon. Wea. Rev.*, **117,** 273-304.